The *Drosophila* Afadin and ZO-1 homologues Canoe and Polychaetoid act in parallel to maintain epithelial integrity when challenged by adherens junction remodeling

Lathiena A. Manning[a], Kia Z. Perez-Vale[b], Kristina N. Schaefer[b], Mycah T. Sewell[a], and Mark Peifer[a,b,c,*]

[a]Department of Biology, [b]Curriculum in Genetics and Molecular Biology, and [c]Lineberger Comprehensive Cancer Center, University of North Carolina at Chapel Hill, Chapel Hill, NC 27599

ABSTRACT **During morphogenesis, cells must change shape and move without disrupting tissue integrity. This requires cell–cell junctions to allow dynamic remodeling while resisting forces generated by the actomyosin cytoskeleton. Multiple proteins play roles in junctional–cytoskeletal linkage, but the mechanisms by which they act remain unclear. *Drosophila* Canoe maintains adherens junction–cytoskeletal linkage during gastrulation. Canoe's mammalian homologue Afadin plays similar roles in cultured cells, working in parallel with ZO-1 proteins, particularly at multicellular junctions. We take these insights back to the fly embryo, exploring how cells maintain epithelial integrity when challenged by adherens junction remodeling during germband extension and dorsal closure. We found that Canoe helps cells maintain junctional–cytoskeletal linkage when challenged by the junctional remodeling inherent in mitosis, cell intercalation, and neuroblast invagination or by forces generated by the actomyosin cable at the leading edge. However, even in the absence of Canoe, many cells retain epithelial integrity. This is explained by a parallel role played by the ZO-1 homologue Polychaetoid. In embryos lacking both Canoe and Polychaetoid, cell junctions fail early, with multicellular junctions especially sensitive, leading to widespread loss of epithelial integrity. Our data suggest that Canoe and Polychaetoid stabilize Bazooka/Par3 at cell–cell junctions, helping maintain balanced apical contractility and tissue integrity.**

Monitoring Editor
Alpha Yap
University of Queensland

Received: Apr 15, 2019
Revised: May 28, 2019
Accepted: May 30, 2019

This article was published online ahead of print in MBoC in Press (http://www.molbiolcell.org/cgi/doi/10.1091/mbc.E19-04-0209) on June 12, 2019.

Author contributions: L.A.M., K.Z.P.-V., and M.P. conceived the study; L.A.M. directed the project; L.A.M. and K.Z.P.-V. analyzed *cnoS-RNAi* and *cno pyd* mutants; K.N.S. and L.A.M. analyzed dorsal closure; L.A.M. and M.T.S. developed RNAi approaches; M.P. analyzed cuticle phenotypes; L.A.M., K.Z.P.-V., and M.P. wrote the manuscript with input from the other authors.

*Address correspondence to: Mark Peifer (peifer@unc.edu).

Abbreviations used: AJ, adherens junctions; AP, anterior–posterior; Arm, Armadillo; Baz, Bazooka; Cno, Canoe; DV, dorsal–ventral; Ecad, E-cadherin; Ena, Enabled; LE, leading edge; MDCK, Madin–Darby canine kidney; Pyd, Polychaetoid; shRNA, short hairpin RNA; SIM, structured illumination microscopy; ZO, zonula occludens.

INTRODUCTION

Building the animal body and maintaining tissue homeostasis require the coordinated effort of many cells acting in concert. Cells must change shape and move, but need to do so without disrupting tissue integrity. These dual needs require integration of the cell adhesion and actomyosin cytoskeletal machinery, which work together to provide cells, tissues, and organs with the correct architecture and allow them to change shape and move in coordinated ways (Heer and Martin, 2017). Epithelial cells, a polarized cell type that act as the building blocks for most tissues, must coordinate adhesion and the cytoskeleton during tissue development. These cells are organized into sheets with apical–basal polarity and are connected by intercellular adhesion complexes. Cadherin-based adherens junctions (AJs) provide connections between cells and form the boundary between the apical and basolateral domains.

Transmembrane cadherins mediate cell–cell adhesion, while p120-catenin, β-catenin, and α-catenin, bound to the cadherin cytoplasmic tails, stabilize cadherins at the cell surface and interact with the actomyosin cytoskeleton (Meng and Takeichi, 2009; Mege and Ishiyama, 2017). Disruption or dysregulation of AJs leads to disorganization of tissue architecture, which is a common step in solid tumor metastasis and numerous developmental disorders.

These vital roles of AJs have made them the subject of intensive research. In the conventional model, cadherins link directly to actin via α- and β-catenin (Rimm *et al*., 1995; Ozawa, 1998). However, more recent work has revealed that this linkage is mediated by a far more sophisticated set of molecules (Mege and Ishiyama, 2017). This led to the search for additional linker proteins that regulate epithelial cell adhesion and AJ/cytoskeletal linkage. One such junction-linker protein is fly Canoe (Cno) and its mammalian homologue Afadin. Cno's multidomain structure allows it to interact directly with the cytoskeleton via its F-actin-binding domain and to bind AJ proteins, including E-cadherin and α-catenin, via its PDZ and proline-rich domains (Miyamoto *et al*., 1995; Mandai *et al*., 2013).

We initially hypothesized that *Drosophila* Cno would be essential for cell adhesion, as was observed for E-cadherin (Ecad; Tepass *et al*., 1996), α– (Sarpal *et al*., 2012), and β-catenin (Cox *et al*., 1996). However, to our surprise, *cno* maternal/zygotic mutants (*cnoMZ*) maintain epithelial integrity throughout gastrulation (Sawyer *et al*., 2009), unlike embryos lacking Ecad or the catenins. Instead, our analysis revealed that while Cno is not essential for maintaining cell–cell adhesion, it is required for many morphogenetic movements requiring AJ/cytoskeletal linkage, including apical constriction and subsequent internalization of the mesoderm, effective cell intercalation during germband elongation, and dorsal closure (Miyamoto *et al*., 1995; Boettner *et al*., 2003; Sawyer *et al*., 2009, 2011; Choi *et al*., 2011). In the absence of Cno, the actomyosin cytoskeleton detaches from AJs, consistent with a role as a linker. This is particularly striking during germband extension, which is largely driven by coordinated opposing planar polarity of AJs/Bazooka (Baz; the fly Par3 homologue) and the actomyosin cytoskeleton, promoting polarized contractility across the entire tissue in the direction of elongation (reviewed in Vichas and Zallen, 2011; Harris, 2018). Loss of Cno enhances AJ and Baz planar polarity on dorsal–ventral cell boundaries and simultaneously leads to retraction of the actomyosin cytoskeleton from the anterior–posterior cortex (Sawyer *et al*., 2011). *cno* and *baz* mutants exhibit strong genetic interactions, consistent with a mechanistic connection (Sawyer *et al*., 2011). An additional role for Cno in later epidermal integrity is suggested by its cuticle phenotype, with the ventral epidermis most sensitive to disruption (Sawyer *et al*., 2009). This special sensitivity of the ventral epidermis is shared in several situations involving reduction in AJ (Tepass *et al*., 1996) or apical polarity proteins (Harris and Tepass, 2008). We explore the mechanistic basis for Cno's role in this process here.

Another potential set of junction–-cytoskeletal linker proteins are those of the Zonula occludens (ZO-1) family. Like Cno, these are multidomain scaffolding proteins that can directly bind F-actin and bind a wide variety of junctional proteins (Fanning and Anderson, 2009). ZO-1 family members are best known for their roles in tight junctions, which in mammals localize just apical to the AJ (Van Itallie and Anderson, 2014). In tight junctions, strands of claudins are positioned apically and cross-linked to the actin cytoskeleton by ZO-1, providing an epithelial barrier. In the absence of ZO-1 family function, claudin strands disperse all along the lateral membrane and barrier function is disrupted (Umeda *et al*., 2006). ZO-1 family proteins also localize to nascent Ajs, where they are thought to have roles in accelerating AJ assembly (Ikenouchi *et al*., 2007; Yamazaki *et al*., 2008). Mice have three ZO family members, with partially overlapping expression patterns. Loss of function mutants in ZO-1 (Katsuno *et al*., 2008) and ZO-2 (Xu *et al*., 2008) have distinct embryonic lethal phenotypes, suggesting partial redundancy. *Drosophila* has only a single family member, Polychaetoid (Pyd; Takahisa *et al*., 1996). However, *Drosophila* lacks apical tight junctions, and Pyd localizes to AJs throughout development (Wei and Ellis, 2001; Jung *et al*., 2006; Seppa *et al*., 2008; Choi *et al*., 2011). We were surprised to learn that *pyd* maternal/zygotic null mutants can survive to adulthood, with defects in Notch signaling that affect bristle development (Choi *et al*., 2011; Djiane *et al*., 2011). However, 60% of maternal/zygotic mutant embryos die, with defects in cell shape change during dorsal closure and defects in tracheal development. Thus, neither Cno nor Pyd alone is essential for early epithelial integrity. Intriguingly, although Afadin and ZO-1 localize to distinct, though adjacent, junctions in mammalian cells, they can physically interact with each other in both mammals and *Drosophila*, and early studies of weak alleles in *Drosophila* indicate a potential synergistic interaction (Yamamoto *et al*., 1997; Takahashi *et al*., 1998). However, because neither allele used in these experiments was a null allele, it was impossible to distinguish whether Cno and Pyd work together in the same process or work in parallel.

Our studies of Cno's homologue Afadin in mammalian Madin–Darby canine kidney (MDCK) cells provided another set of insights (Choi *et al*., 2016). In these cells, reducing Afadin levels has only subtle effects. Reducing levels of ZO-1 family members, in contrast, stimulates robust assembly of a contractile actomyosin array at the apical adherens junction (Fanning *et al*., 2012) via activation of Shroom and Rho kinase (Choi *et al*., 2016). In these cells, each cell border, bounded by tricellular junctions, serves as an independent contractile unit. Borders are contractile, but within homeostatic limits, as balanced contractility between different cell borders maintains individual cell borders at roughly similar lengths, and thus cell shape is relatively homogeneous. Knockdown of Afadin in this ZO-1 knockdown background strikingly disrupted this homeostatic balance, leading to highly unbalanced contractility. Some cell borders became shortened and hypercontractile, while others became hyperelongated. Disruptions in the actomyosin cytoskeleton at cell junctions were most readily apparent at tricellular and multicellular junctions, where the tight bundling of actin and myosin in the AJs was lost. However, these disruptions could spread into neighboring bicellular borders. These data suggested that Afadin and Cno may play an additional role in helping maintain balanced contractility at different cell borders, and thus maintain epithelial integrity.

Cno's diverse functions in embryonic development mean that the early effects of its loss make it challenging to assess whether effects later are primary or secondary. We thus developed RNAi tools to reduce Cno function to different extents. We also developed methods for simultaneously reducing the function of Cno and Pyd, to explore whether they act together or in parallel in epithelial tissues. This revealed important roles for Cno in balancing contractility at different cell borders throughout development and suggests that Cno and Pyd/ZO-1 act in parallel in maintaining adhesion and junctional integrity during morphogenesis.

RESULTS

Developing tools to titrate reduction of Canoe function, allowing exploration of its full range of roles in embryonic development

cno was originally identified in *Drosophila* through the effect of zygotic mutants on dorsal closure (Jürgens *et al*., 1984; Miyamoto *et al*., 1995; Choi *et al*., 2011). The zygotic null mutant has relatively

mild defects during this process, since these embryos retain at least some maternally contributed Cno through dorsal closure (Choi *et al.*, 2011). Later studies of maternal/zygotic loss of *cno* (*cnoMZ*), in which Cno expression was completely removed, revealed important roles of Cno in mesoderm invagination and germband elongation (Sawyer *et al.*, 2009, 2011). These studies also suggested that Cno regulates the link between AJ and actin during apical constriction. We suspected that Cno also played important subsequent roles. Analysis of the *cnoMZ* cuticle phenotype (Sawyer *et al.*, 2009) suggested a later role in epidermal integrity, but the mechanisms by which it acts in maintaining epidermal integrity were not known. In addition, the severity of the *cnoMZ* terminal phenotype made studying its role in late embryonic events such as dorsal closure difficult, as it is hard to distinguish between primary and secondary consequences of Cno loss.

To explore Cno's roles in the full set of developmental events in which it is involved, we hypothesized that utilizing RNA interference (RNAi) in conjunction with the Gal4-UAS system (Brand and Perrimon, 1993; Duffy, 2002) would allow us to titrate Cno knockdown to different levels in order to study a wider variety of postgastrulation events. The TRiP project has generated lines expressing shRNAs under the control of Gal4 drivers against many *Drosophila* genes (Perkins *et al.*, 2015), including *cno* (Bonello *et al.*, 2018), allowing efficient knockdown. The community has also generated a wide variety of lines expressing GAL4 in different tissues and at different times. Among these are lines expressed during midoogenesis, allowing knockdown of maternally contributed mRNAs and continued knockdown of zygotic mRNAs in the progeny (Staller *et al.*, 2013). The strongest of these can result in a maternal/zygotic null phenotype. In an effort to obtain different degrees of Cno knockdown, we generated females carrying one of three different maternal Gal4 drivers, along with the *UAScnoRNAiValium20shRNA* or *UAScnoRNAiValium22shRNA* constructs, and tested their phenotypes. Our tests ordered these maternal drivers into the relatively weak *nos-Gal4,* the moderate *MTD-Gal4 driver*, and the strong "*mat-Gal4-2+3*" driver carrying maternal α-tubulin-GAL4 drivers on both the second and third chromosomes (*shRNA* and *GAL4* lines used are described in detail in Table 2 in *Fly stocks* later in this article).

As an initial screen of how different degrees of Cno knockdown affect morphogenesis, we assessed embryo lethality and cuticle phenotype, as the latter reveals the success of major morphogenetic movements and the effect on epidermal integrity. We created categories to illustrate the range of morphogenic phenotypes seen in different *cno* mutant or knockdown genotypes (Figure 1, A–I). Head involution is most sensitive to Cno reduction (Figure 1, A–C), with defects in dorsal closure seen after moderate reduction

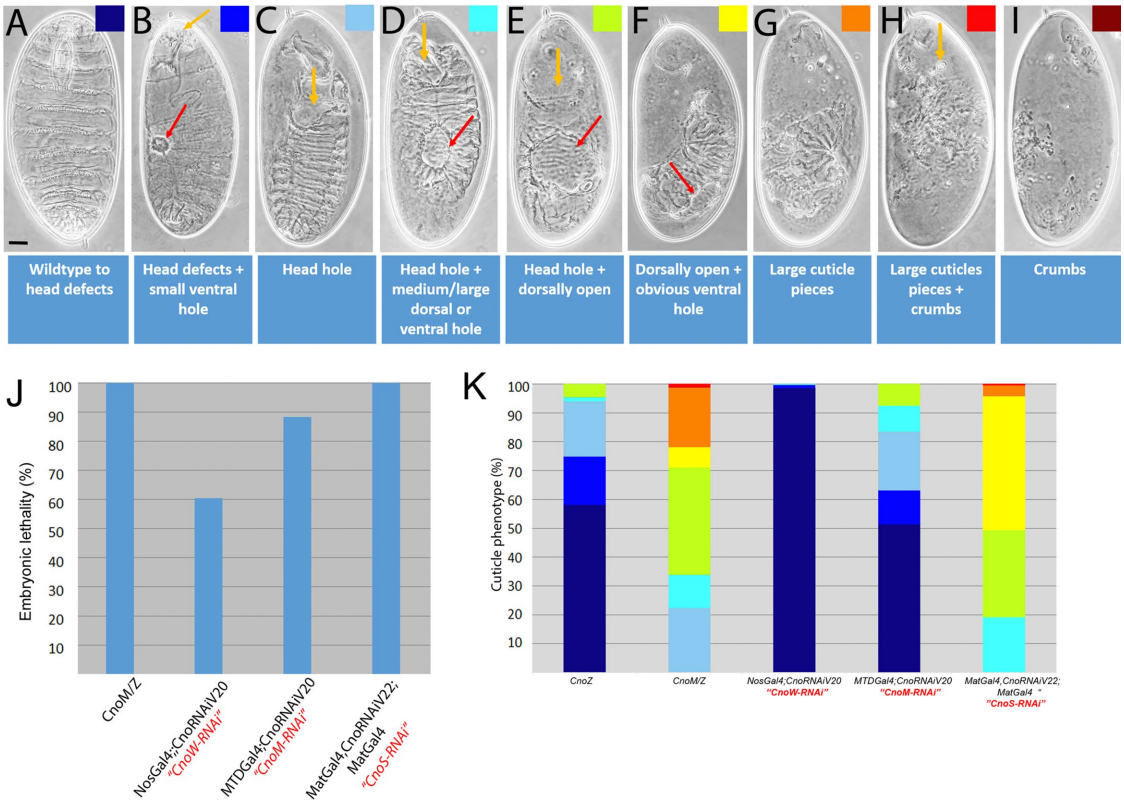

FIGURE 1: Developing tools to modulate Cno function using RNAi. (A–I) Cuticle preparations revealing the spectrum of defects in morphogenesis and epithelial integrity seen in embryos with different degrees of Cno function. (A) Nearly wild-type cuticle with subtle defects in the head skeleton (arrow). Scale bar = 30 μm. (B) Defects in head involution are accompanied by small holes in the ventral or dorsal cuticle (red arrow). (C) Failure of head involution, leaving a hole in the anterior (yellow arrow). (D) Failure of head involution (yellow arrow) accompanied by a large hole in the ventral or dorsal cuticle (red arrow). (E) Failure of both head involution (yellow arrow) and dorsal closure (red arrow). (F) Dorsally open with hole in the remaining cuticle (arrow). (G) Remaining cuticle in large fragments. (H) Large and small fragments of cuticle (crumbs-like; yellow arrow). (I) Only small cuticle fragments remaining. (J) Embryonic lethality of different *cno* RNAi genotypes relative to cno^{R2} maternal/zygotic mutants (*cnoM/Z*). (K) Severity of cuticle phenotypes of different *cno* RNAi genotypes relative to cno^{R2} zygotic (*cnoZ*) or maternal/zygotic mutants.

Genotype	Wild type or minor head defects (%)	Head defects + small ventral hole (%)	Head hole (%)	Head hole + medium/ large dorsal or ventral hole (%)	Head hole + dorsally open (%)	Totally dorsal open + obvious ventral hole (%)	Large cuticle pieces (%)	Large cuticle pieces + crumbs (%)	Crumbs only (%)	Total	Lethality (%)
cno^{R2} zygotic null (*CnoZ*)	58	17	19	1.50	5.00	0	0	0	0	131	100
cno^{R2} maternal and zygotic (*MZ*) null	3	1	21	11	36	7	20	1	0	253	100
NosGal4; *cnoV20shRNA* (weak = *cnoW-RNAi*)	99	1	0	0.30	0	0	0	0	0	367	61
MTDGal4; *cnoV20shRNA* (moderate = *cnoM-RNAi*)	51	12	20	9	7.50	0	0	0	0	333	88
MatGal4; *cnoV20shRNA* (control cross for double mutant)	21	2	18	23	25	8	2	2	0	665	84
MatGal4; MatGal4/*cnoV22shRNA* (strong = *cnoS-RNAi*)	0	0	0.20	19	30	46	4	0.40	0	521	100
pyd^{B12}/*pyd*^{B12} *CnoV20shRNA* (*pyd cno* mutant)	0.20	0	5	13	13	22	23	19	5	471	100

TABLE 1: Cuticle phenotypes.

(Figure 1, D–F), and finally defects in epidermal integrity observed in the strongest mutant combinations (Figure 1, G–I). As our baselines for comparison, we used *cno* zygotic null mutants (zygotic *cno*^{R2}/*cno*^{R2}; Sawyer *et al*., 2009), which retain maternally contributed Cno, and maternal/zygotic *cno*^{R2}null mutants (*cnoMZ;* Sawyer *et al*., 2009), which completely lack Cno. Zygotic null mutants exhibit fully penetrant embryonic lethality, but defects in morphogenesis are relatively mild, ranging from mild to strong defects in head involution (Figure 1K; Table 1; Sawyer *et al*., 2009). At the other end of the phenotypic spectrum, *cnoMZ* mutants also exhibit complete embryonic lethality (Figure 1J; $n = 432$) but cuticle defects are much more severe, with most embryos exhibiting complete failure of both head involution and dorsal closure and many with more severely disrupted epidermal integrity (Figure 1K; Table 1; Sawyer *et al*., 2009).

Our different *cno* RNAi strategies delivered a wide range of phenotypes, from embryos with no observable defects to those with severe morphogenic defects such as those seen in *cnoMZ*. The vast majority of embryos in which our weak *nos-Gal4* drove *UAS-CnoRNAi20shRNA* (*cnoW-RNAi)* exhibited largely normal cuticle morphology, with virtually all having only minor head defects (Figure 1K; Table 1), and 39% of the embryos were viable ($n = 171$; Figure 1J). The moderate *MTDGal4* driving *UASCnoRNAi20shRNA* (referred to below as *cnoM-RNAi*) led to more penetrant embryonic lethality (88%, $n = 330$; Figure 1J) and provided the broadest spectrum of cuticle phenotypes. Half of the progeny had mild head defects and half had strong disruption of head involution and mild effects on dorsal closure (Figure 1K; Table 1). The strongest GAL4/RNAi combination, *mat-Gal4-2+3* driving *UASCnoRNAi22shRNA* (below referred to as *cnoS-RNAi*), had completely penetrant lethality (100%; $n = 389$; Figure 1J) and the strongest embryonic defects, with 30% exhibiting the "canoe" phenotype, reflecting complete failure of head involution and dorsal closure (Figure 1F), and 50% having additional defects in epidermal integrity (Figure 1K). *cnoS-RNAi* embryos had Cno reduced to essentially undetectable levels at the onset of development (to 1.3% of wildtype; Supplemental Figure 1, A and B), and Cno levels remained drastically reduced at the end of morphogenesis (to 4.9% of wildtype; Supplemental Figure 1, A and C). Analysis by immunofluorescence confirmed these reductions (Supplemental Figure 1, G′ vs. H′). *cnoS-RNAi* largely phenocopied the maternal/zygotic loss of Cno, as assessed by cuticle pattern (Figure 1K). Together, this set of UAS-RNAi/GAL4 lines provided us with the ability to dial Cno function down to the desired degree to study different embryonic events. In subsequent analysis, we used *cnoS-RNAi* to analyze earlier embryonic events beginning during and just after germband extension, allowing us to explore the genesis of epithelial integrity defects, and focused on the moderate *cnoM-RNAi* in studies examining the role of Cno in dorsal closure.

Canoe is required to maintain homeostatic cell shapes and balanced contractility along the leading edge during dorsal closure

Our recent superresolution imaging in cultured mammalian MDCK cells suggested that Cno's homologue Afadin plays a prominent role at tricellular and multicellular junctions where three or more cells meet, reinforcing end-on links between the actomyosin cytoskeleton and cell–cell junctions and thus allowing tricellular junctions to resist mechanical tension generated by actomyosin contractility along the cell border (Choi *et al*., 2016). These data fit with our earlier work in *Drosophila*, which revealed that Cno is enriched at tricellular junctions and strengthens actomyosin–junction linkages during mesoderm invagination and

germband elongation (Sawyer *et al.*, 2009, 2011; Bonello *et al.*, 2018).

We sought to explore Cno's role at tricellular and multicellular junctions further in vivo. Dorsal closure provides a superb place to study this, as the dorsalmost cells of the lateral epidermis assemble a planar-polarized contractile actomyosin cable at their leading edges, anchored cell to cell at tricellular junctions that join cells of the lateral epidermis to one another and to cells of the abutting amnioserosa. Contraction of this supercellular cable, along with pulsed contractions of the more dorsal amnioserosal cells, help power closure (reviewed in Hayes and Solon, 2017; Kiehart *et al.*, 2017). Previous analyses of Cno's role in dorsal closure relied on zygotic *cno* mutants (e.g., Boettner *et al.*, 2003; Choi *et al.*, 2011). However, most zygotic null mutants complete closure due to maternally contributed protein (Sawyer *et al.*, 2009; Figure 1), and thus the phenotype we observed does not reveal Cno's full role in this process.

Our new set of RNAi tools allowed us to dial down Cno function to a level at which dorsal closure could be initiated, but at which Cno function was substantially lower than that seen in zygotic *cno* mutants (Figure 1K). To do so, we drove the *cnoV20shRNA* with the maternal triple driver (MTD) GAL4 (Mazzalupo and Cooley, 2006; *cnoM-RNAi*). Embryos that received two copies of the hairpin had substantial defects in head involution and dorsal closure (Figure 1, A–I and K). We thus began by examining embryos during these stages stained with antibodies against AJ and cytoskeletal proteins, to allow us to assess morphogenetic movements and cell shape change during dorsal closure.

Wild-type dorsal closure begins at the completion of germband retraction. The scalloped boundary between the epidermis and amnioserosa (Figure 2A, red arrows) straightens (Figure 2, B and I, red arrows) as the actin cable is assembled. Epidermal cells elongate along the dorsal–ventral axis, beginning with those at the leading edge (LE; Figure 2A, inset) and then the more ventral cells (Figure 2, B and I). The forces generated by amnioserosal cell apical constriction and the contractile actomyosin cable assembled at the leading edge combine to gradually close the dorsal opening (Kiehart *et al.*, 2000; Hutson *et al.*, 2003; Figure 2, B–D). As the two sheets meet at the anterior and posterior canthi, they zipper together (Figure 2, C and D, red arrows) until the opening is closed and the embryo is completely enclosed in epidermis. At that point the amnioserosal cells undergo apoptosis (Toyama *et al.*, 2008). Head involution occurs in parallel (Figure 2, B–D, yellow arrows). In contrast, morphogenesis was severely altered in *cnoM-RNAi* embryos. They exhibited strong defects in head involution, with the head epidermis lost or disrupted (Figure 2, E–H vs. A–D, yellow arrows), and germband retraction was not completed (Figure 2, F and G vs. B and C, green arrows). Some defects observed were similar to those previously observed in *cno* zygotic null mutants (Choi *et al.*, 2011), such as the retention of excessively deep segmental grooves (Figure 2, F–H vs. D, blue arrows) and an LE that was wavy rather than straight (Figure 2, J vs. I). However, other defects were much more severe. Unlike wild-type embryos, where zippering of the two epidermal sheets is complete before the amnioserosa undergoes apoptosis, in many *cnoM-RNAi* embryos, the two epidermal sheets remained far apart when the amnioserosa began apoptosis, leaving the underlying muscle and gut tissues exposed (Figure 2, F–H, white arrows).

The LE provides a superb place to assess Cno's mechanisms of action. LE cells assemble a planar polarized actomyosin cable at their dorsal margin, where they contact the amnioserosal cells (Figure 3, A–E). In wild type the cable initially assembles at the onset of dorsal closure (Figure 3A) and is maintained and enhanced as closure proceeds (Figure 3, B and C). The cable behaves in a supercellular manner, exerting force all along its length (Kiehart *et al.*, 2000; Hutson *et al.*, 2003). To accomplish this, individual cell cables (Figure 3D, white arrows) must be connected cell to cell, presumably at cadherin-based AJs (Figure 3D, blue arrows). Consistent with this, Ecad is particularly enriched at the LE tricellular junctions (Figure 3E; Kaltschmidt *et al.*, 2002), at the location where individual cell actin cables are presumably anchored. Cno is also somewhat enriched at these locations (Figure 3F; Kaltschmidt *et al.*, 2002), reminiscent of its enrichment at tricellular junctions earlier in embryogenesis (Sawyer *et al.*, 2009; Bonello *et al.*, 2018). In our earlier work we also identified a distinctive localization for the actin polymerization regulator Enabled (Ena) at these special tricellular junctions (Gates *et al.*, 2007; Choi *et al.*, 2011; Nowotarski *et al.*, 2014). In vitro, Ena localizes to growing (barbed) ends of actin filaments (reviewed in Edwards *et al.*, 2014). Ena is required for effective cell shape change during dorsal closure (Gates *et al.*, 2007). Ena is enriched at all tricellular junctions during the extended germband stage (Gates *et al.*, 2007). As dorsal closure begins, it remains at tricellular junctions of all epidermal cells (e.g., Figure 4A, yellow arrow), but becomes particularly enriched at LE tricellular junctions (Figure 4A, blue arrows) and at the borders of segmental groove cells (Figure 4A, red arrow). As closure proceeds, Ena enrichment at the LE tricellular junctions continues to increase (Figure 4, B and C, arrows). The LE thus provides a place to test our hypothesis, based on our earlier work in *Drosophila* embryos and in knockdown MDCK cells, that Cno and Afadin are cytoskeletal-junction cross-linkers that reinforce connections under tension and that may also help balance tension between different borders.

We first sought a more detailed understanding of the molecular architecture at the LE, to help us better interpret both the process of wild-type dorsal closure and the effects of reducing Cno. We thus turned to structured illumination microscopy (SIM), using the improved resolution to more precisely define how Cno, Ecad, actin, myosin, and Ena are arrayed along the LE relative to one another in three dimensions (3D) (Figure 5; our methodology for processing images obtained by SIM is in Supplemental Figure 2). Standard confocal imaging usually visualized a single Ena "dot" at each tricellular junction (Figure 4C'), but use of the Zeiss Airyscan module occasionally resolved these into pairs of dots flanking the cadherin-based AJs (Figure 4D). SIM imaging allowed us to better resolve the Ena "dots." SIM usually resolved the single Ena dot seen in confocal microscopy into a more complex bipartite structure (Figure 5, B–D), with Ena dots (blue arrows) flanking each side of the Ecad concentrations at the LE tricellular junctions. Viewing these in the *Z*-axis revealed that Ena aligns with the AJs proteins precisely along the apical–basal axis (Figure 5E). Imaging Ena together with Cno (Figure 5, F–I) revealed a similar picture, with Ena flanking Cno at LE tricellular junctions (Figure 5, G–I, blue arrows). We next imaged Ena along with F-actin (Figure 5, J–M). This revealed that the paired Ena dots (Figure 5, K and L, blue arrows) localized to the tricellular junction-proximal ends of the actin cables (magenta arrows) that run along the LE. Once again, Ena also aligned with the ends of the actin cable along the apical–basal axis (Figure 5M). Given the known properties of Ena/VASP proteins, this may suggest that actin barbed ends concentrate where the cable interfaces with the cadherin–catenin complex. Finally, our SIM imaging confirmed something that was previously suggested from confocal imaging (e.g., Franke *et al.*, 2005): myosin is strongly enriched on the central regions of each actin cable and absent or at reduced levels closest to the LE tricellular junctions (Figure 5, N–R).

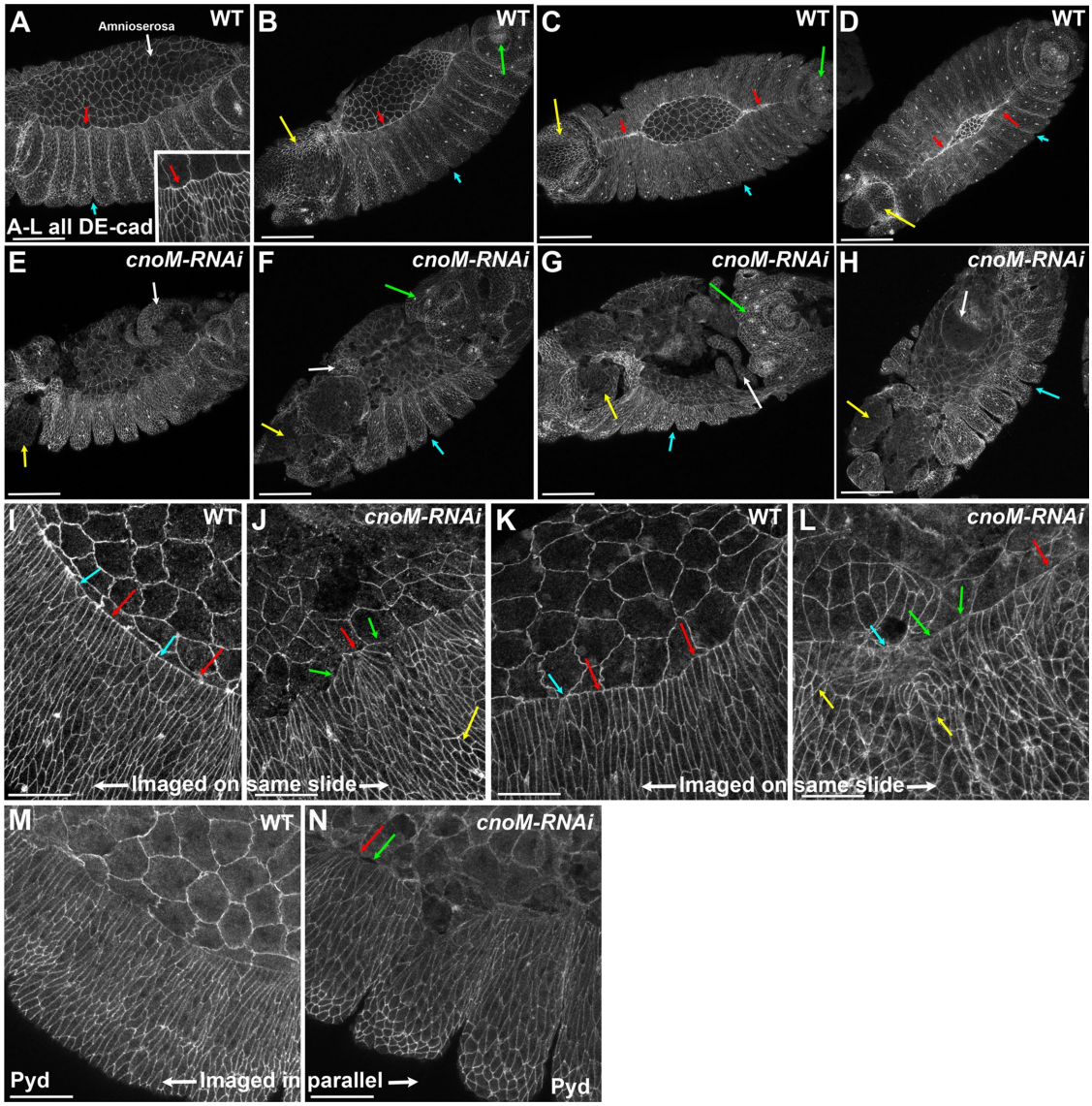

FIGURE 2: Moderate Cno knockdown disrupts dorsal closure and leads to uneven cell shapes along the leading edge. Embryos, stage 13–14, genotypes indicated. All images show Ecad except M and N, which show Pyd. (A–D) Wild type, progression through dorsal closure. (A) At onset the leading edge is scalloped (red arrows), and segmental grooves remain relatively deep (blue arrow), extending to the leading edge. (B–D) As closure proceeds, the leading edge straightens; B, red arrow. This occurs simultaneously with head involution (yellow arrows). The two epidermal sheets zipper together at the canthi; C, D, red arrows. The posterior spiracles have fully retracted to the posterior end (green arrows), and the segmental grooves have largely retracted (blue arrows). (E–H) *cnoM-RNAi* embryos at comparable stages. Head involution has failed (yellow arrows). Segmental grooves remain abnormally deep (blue arrows). Germband retraction has not been completed in many embryos (green arrows), and holes appear in the amnioserosa, exposing underlying tissue (white arrows). (I–N) Cell shapes at the leading edge. (I, K, M) In the wild type, cells are largely uniformly elongated along the dorsal–ventral axis and in width along the leading edge (red arrows), with the exception of cells making the segmental grooves (blue arrows). (J, L, N) *cnoM-RNAi*. Leading edge cell shapes are highly irregular: some cells have hyperconstricted (red arrows) or hyperelongated (green arrows) leading edges. A subset of cells behind the leading edge fail to elongate along the dorsal–ventral axis (yellow arrows). I vs. J, K vs. L, and M vs. N were imaged on the same slide or in parallel, revealing no dramatic changes in Ecad or Pyd cortical localization. Scale bars: A–H = 50 μm and I–N = 20 μm.

These data informed our analysis of the cell biological consequences of strong Cno reduction for cell shape, the actomyosin cable, and its attachment to the LE cell junctions. Assembling the LE cable puts the LE under tension due to cable contractility (e.g., Kiehart *et al.*, 2000; Jacinto *et al.*, 2002), with cells exerting force on their neighbors along the cable. In the wild type, this tension is balanced, as assessed by the relatively uniform cell widths of different cells along the LE (Figure 2, I and K, red arrows). There is some variability, but it is largely confined to cells near the former segmental grooves (Figure 2I, blue arrows). In contrast, in most *cnoM-RNAi* embryos, LE cell width is *much* more variable, with the LE of some cells hyperconstricted (Figure 2, J and L, red arrows) while in other cells the LE is hyperelongated (Figure 2, J and L, green arrows). The degree of cell elongation along the dorsal–ventral axis was also much

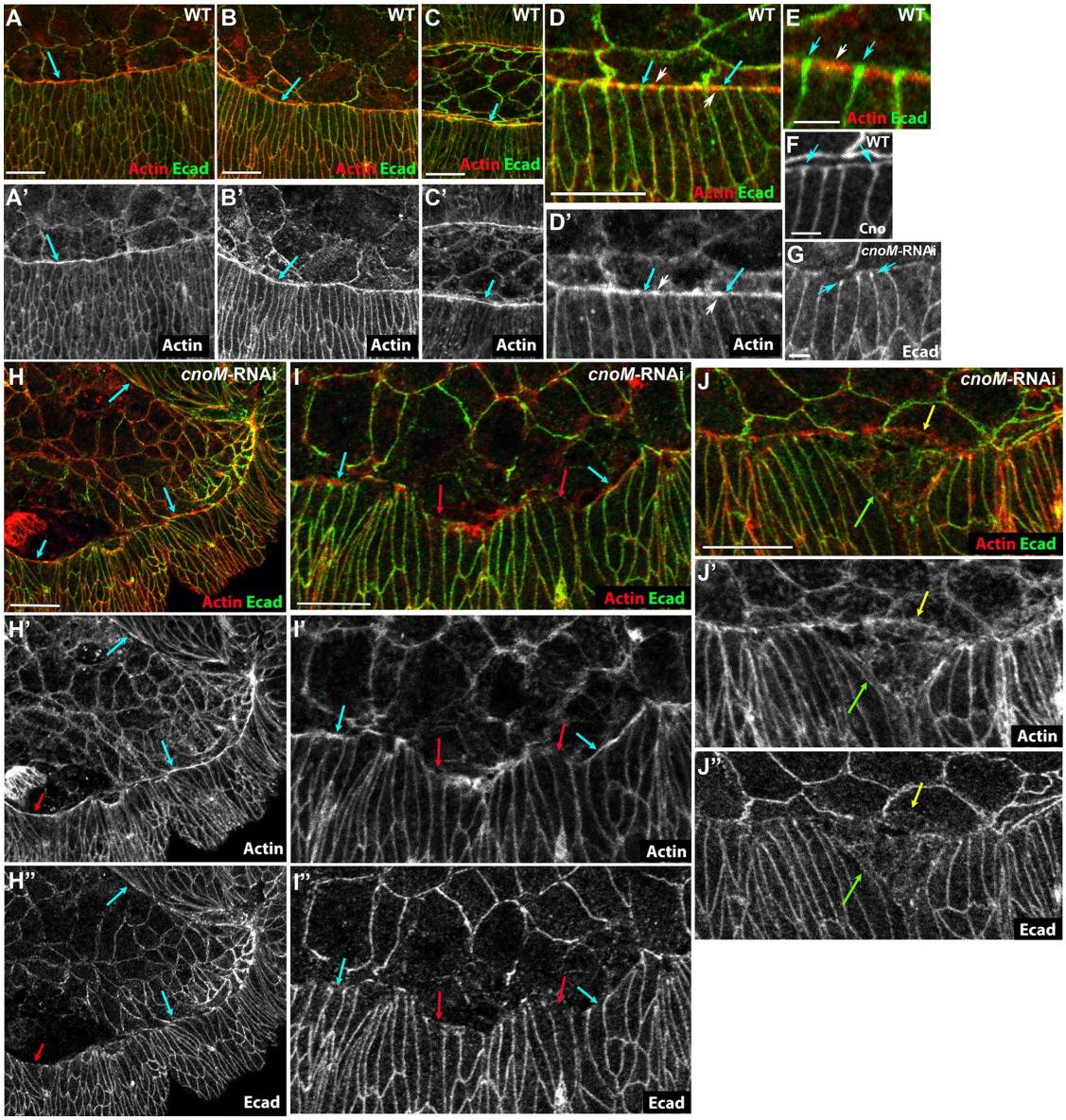

FIGURE 3: Moderate Cno knockdown does not prevent actin cable assembly but does lead to irregularity in cable maintenance. Embryos, stage 13–14, genotypes indicated. All images show Ecad and actin (imaged with phalloidin), except F, which shows Cno. (A–F) Wild type. (A–C) Progression through dorsal closure. Actin cable intensifies (blue arrows). (D–F) Actin cable (white arrows) is linked cell to cell at leading edge tricellular junctions, where both Ecad and Cno are enriched (blue arrows). (G–J) *cnoM-RNAi* embryos. (G) Ecad enrichment at leading edge AJs is not lost. (H–J) The actin cable can be assembled and maintained, even by cells in which the leading edge is hyperextended (blue arrows), but discontinuities in the cable (red arrows) and leading edge cell ripping (J, yellow vs. green arrows) were observed. Scale bars in E–G = 2 μm. All other panel scale bars = 10 μm.

more variable, and some cells failed to elongate (Figure 2, J and L, yellow arrows). This data and previous studies of Afadin knockdown in MDCK cells under tension (Choi *et al*., 2016) suggest that Cno/Afadin may help ensure balanced contractility on different cell borders.

We next examined whether cells retained the ability to assemble a planar-polarized actin cable after reduction of Cno. Strikingly, even the most severely affected *cnoM-RNAi* embryos retained at least a partial LE actin cable (Figure 3H, arrows). In less affected embryos (presumably those inheriting a single copy of the shRNA), the actin cable appeared relatively normal. In embryos with more dramatically altered LE cell shapes, the cable was discontinuous (Figure 3I, red arrows), though surprisingly, even some cells in which the LE was very splayed open retained an actin cable (Figure 3, I–I′, blue arrows). When the LE cells separated from the amnioserosa, the cable could remain intact (Figure 3H′, red arrow), but more often the LE cell itself seemed to be ripped apart (Figure 3J, green and yellow arrows). Loss of AJs could provide a possible mechanism for cable discontinuity; however, after *cnoM-RNAi*, Ecad levels were not substantially lower than wild type (Figure 2, I vs. J, K vs. L; embryos stained and imaged on the same slide, with wild type marked with histone-GFP), and Ecad continued to be enriched in many LE tricellular junctions (Figure 3G). However, where contact with the amnioserosa was disrupted Ecad localization was also disrupted (Figure 2L, blue arrow, 3J). *cnoM-RNAi* embryos also retained junctional

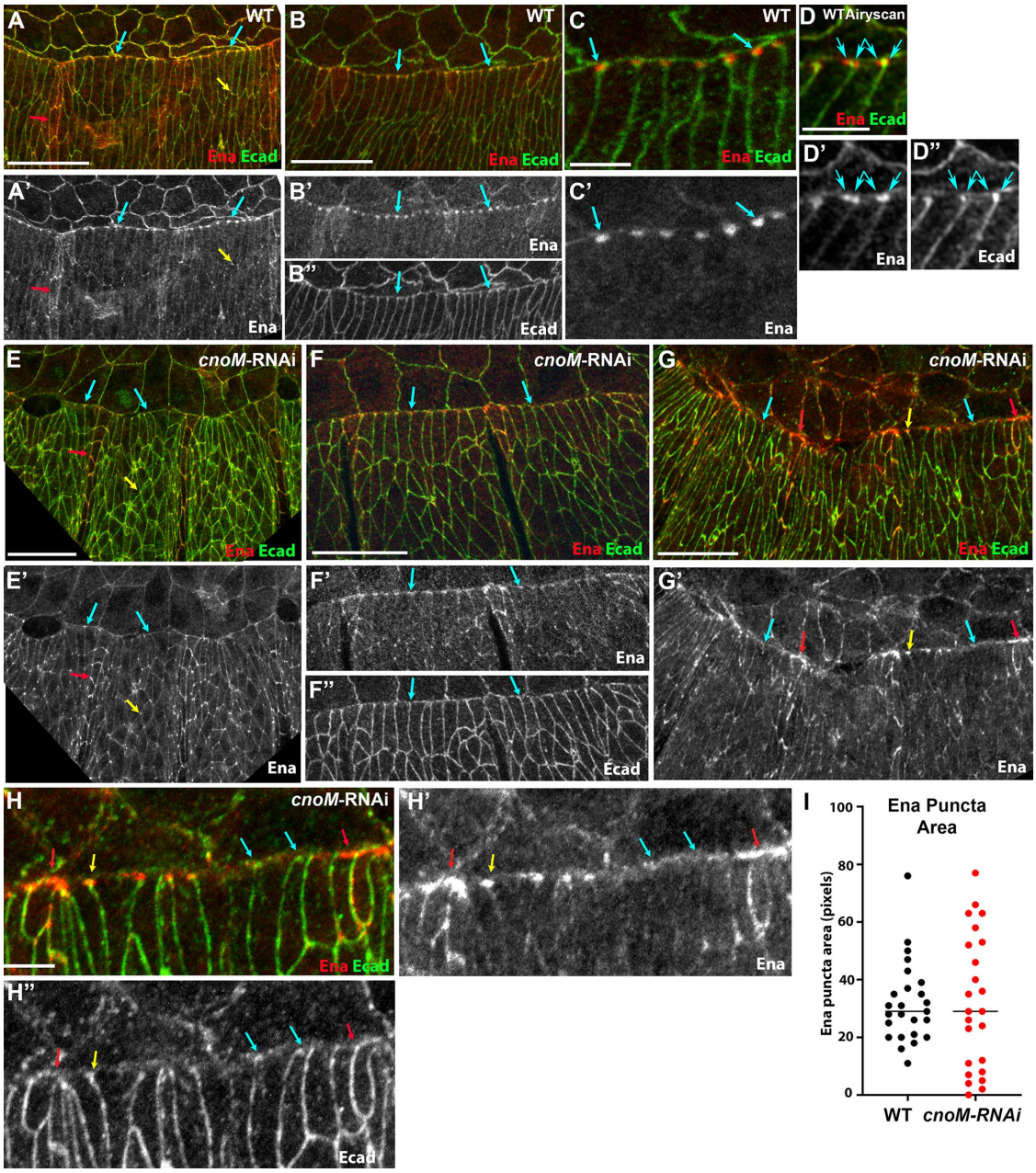

FIGURE 4: Ena localizes adjacent to leading edge AJs and moderate Cno knockdown disrupts this uniform localization. Embryos, stage 13–14, genotypes indicated. All images show Ecad and Ena. (A–D) Wild type. (A) At the onset of dorsal closure, Ena localizes to all epidermal tricellular junctions (e.g., yellow arrow), and is especially enriched in segmental groove cells (red arrow). Enrichment near the leading edge AJs begins (blue arrows). (B, C) As closure proceeds, enrichment next to leading edge AJs increases. (D) Airyscan superresolution image. Leading edge "dots" sometimes resolve into two dots on the two sides of the Ecad. (E–H) *cnoM-RNAi*. (E) Early in closure Ena localization to epidermal tricellular junctions (e.g., yellow arrow) and segmental groove cells (red arrow) are relatively unchanged from wild type, while localization near the leading edge AJs is less uniform (blue arrows). (F) As closure proceeds, leading edge Ena localization is less focused at tricellular junctions than in wild type (arrows; compare with B), even when cell shapes are relatively normal. (G, H) In most embryos, leading edge Ena localization becomes much more irregular. Distinct leading edge dots remain in some cells (yellow), but at many tricellular junctions, Ena localization at leading edge dots is diminished (blue arrows) or broadened (red arrows). (I) Quantification of Ena puncta area at leading edge tricellular junctions. Images were binarized using ImageJ, and areas were measured using the wand tool. Scale bars in A, B, E, F, G = 20 μm. Scale bars in C, D, H = 5 μm.

localization of the AJ protein Pyd (Figure 2M vs. Figure 3N). Thus, Cno is not essential for actin cable assembly or contractility, but it is important for maintaining balanced cell contractility and thus actin cable continuity.

Finally, we examined localization of Ena. Ena is also important for maintaining balanced contractility along the LE and for timely and accurate dorsal closure (Gates *et al.*, 2007). The effects of Ena loss on LE cell shapes are quite similar to those seen after *cnoM-RNAi*. Our

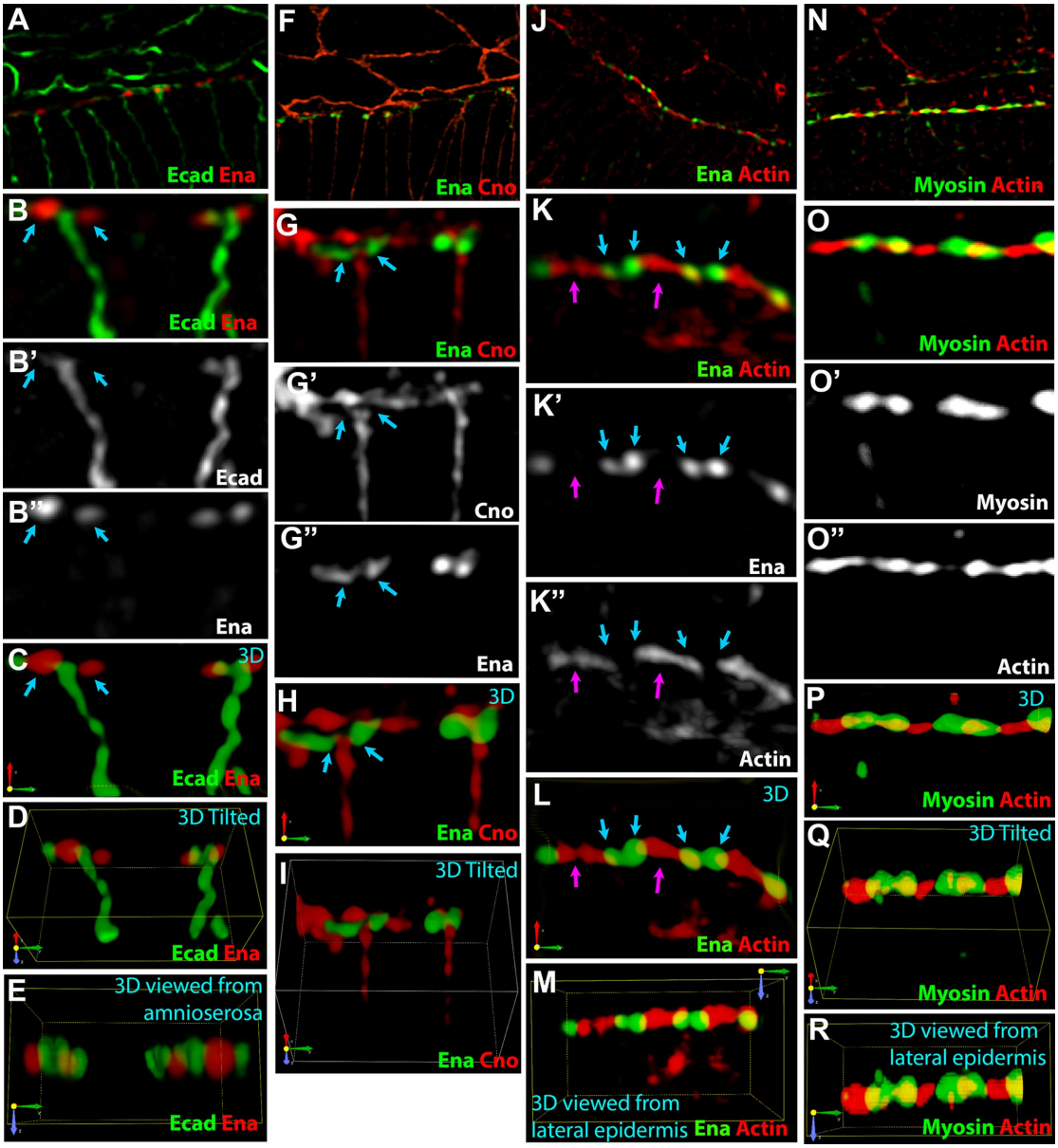

FIGURE 5: SIM superresolution microscopy of the leading edge (LE) actin cable and tricellular junctions. SIM images of wild-type embryos mid–stage 13 (mid–dorsal closure), antigens indicated. Directional arrows indicate X (red), Y (green), and Z (blue) axes. (A–E) Ena and Ecad. (A) Ena puncta (e.g., arrows) flank Ecad at LE tricellular junctions. (B–B″) Two tricellular junctions at the LE. SIM resolves two separate Ena puncta (e.g., arrows) that are juxtaposed and surround Ecad at tricellular junctions. Maximum-intensity projection (M.I.P.) of *z*-stacks. (C) 3D reconstruction of M.I.P. from panel B, using alpha blending. This allows visualization of the LE 3D space. (D) Tilted view of 3D reconstruction. (E) 3D reconstruction from the vantage point of the amnioserosa (rotated 90° from panel C; apical up). Ena and Ecad are in the same plane on the apical–basal axis. (F–I) Cno and Ena. (F) Cno's relationship to Ena parallels that of Ena and Ecad. (G–G″) Ena is juxtaposed to Cno at tricellular junctions. (H) 3D reconstruction. (I) Tilted view of 3D. (J–M) Ena and actin (visualized with phalloidin). (J) Lower magnification view of the LE. (K–K″) SIM resolves Ena localization to two separate puncta (blue arrows) located at the ends of each cell's actin cable (magenta arrows). (L) 3D reconstruction. (M) 3D reconstruction showing view from the lateral epidermis (rotated 90° from L; apical up). Ena and Actin are parallel along the apical–basal axis. (N–R) Zipper (myosin II heavy chain) and actin. (N) Actin and myosin are arranged in an alternating pattern across the LE of the lateral epidermis. (O–O″) Two LE cells. Myosin is enriched in the central portion of each cell's actin cable. (P) 3D view. (Q) Tilted view of 3D reconstruction. (R) 3D reconstruction side view from the lateral epidermis (rotated 90° from panel P; apical up). Myosin and actin are parallel along the apical–basal axis. Scale bars in A, F, J, and N = 20 μm. All others = 2 μm.

previous analysis of *cno* zygotic and *pyd* maternal/zygotic mutants revealed alterations in Ena localization and also revealed genetic interactions between *cno* or *pyd* and *ena* (Choi *et al.*, 2011). Our stronger knockdown tools allowed us to extend this. Early in dorsal closure, *cnoM-RNAi* embryos retained Ena enrichment at lateral epidermal tricellular junctions (e.g., Figure 4, E–E′, yellow arrow) and in segmental groove cells (Figure 4E′, red arrow) but LE enrichment was reduced (Figure 4E′, blue arrows). As closure proceeded, Ena

enrichment became less focused at LE tricellular junctions than in wild type (Figure 4, F–F″, arrows). In the most severely affected embryos, Ena localization became extremely irregular. While occasional tricellular junctions had focused Ena localization (Figure 4, G and H, yellow arrows), Ena was not focused at most tricellular junctions (Figure 4, G and H, red arrows) and was strongly reduced at others (Figure 4, G and H, blue arrows). When we quantified the intensity of Ena puncta at tricellular junctions, it confirmed the greater variability seen along the LE after *cnoM-RNAi* (Figure 4I, analyses based on $n = 25$ [five measurements taken from five embryos per treatment]; $p = 0.0000004$; coefficient of variation = 27% for wild type, 63% for *cnoM-RNAi*). Taken together, our data are consistent with the idea that Cno is important for allowing cell junctions along the LE to resist the contractile force of the actomyosin cable and maintain relatively uniform cell shapes, a role Afadin also plays in MDCK cells (Choi *et al.*, 2016). Our data are consistent with the idea that Ena may also play a role in this, via its position at the junction of the cadherin–catenin complex and the actin cable.

Canoe is critical for cells to retain columnar architecture when challenged by cell division and neuroblast invagination

When we first initiated analysis of Cno a decade ago, we expected that it would play an essential role in cell adhesion, with loss leading to complete disruption of epithelial integrity at gastrulation onset, as is seen in mutants lacking Ecad, β- or α-catenin (Cox *et al.*, 1996; Tepass *et al.*, 1996). However, while many morphogenetic movements of gastrulation are disrupted by Cno loss, the ectoderm initially remains intact (Sawyer *et al.*, 2009, 2011). Cuticle analysis (Figure 1) suggests that epidermal integrity is ultimately reduced but not eliminated, though the underlying mechanisms remained unexamined. We thus set out to determine what role Cno plays in maintaining epithelial integrity and what mechanisms act in parallel when Cno is absent. To do so, we used our strongest *cno* RNAi condition, *cnoS-RNAi* (the crosses and progeny are diagrammed in Supplemental Figure 3), which phenocopies complete loss of Cno and leads to very strong reduction in levels of Cno protein (Supplemental Figure 1, A–C). Cuticle analysis revealed results similar to those seen in embryos maternally and zygotically null for Cno (Figure 1K; Table 1; Sawyer *et al.*, 2009). Head involution and dorsal closure failed, and the thoracic and abdominal epidermis had frequent ventral holes.

We thus examined the progression of epithelial integrity from gastrulation onset to the end of dorsal closure, with a focus on the thorax and abdomen. *cnoS-RNAi* embryos phenocopied *cnoMZ* mutants (Sawyer *et al.*, 2009; Choi *et al.*, 2013), cellularizing despite disruption in initial establishment of apical AJs and beginning gastrulation with an intact ectoderm (Supplemental Figure 4, A vs. B). However, mesoderm invagination was partially to completely disrupted, and extension of the germband was slowed or terminated prematurely (Figure 7F later in the paper; unpublished data). In a subset of embryos (18%; 8/45), the continued intercalation of ectodermal cells combined with the failure to fully extend the germband led to a twisted gastrulation phenotype. In wild-type embryos, germband extension is driven in part by the planar- polarized distribution of junctional and cytoskeletal proteins (reviewed in Vichas and Zallen, 2011; Harris, 2018; illustrated in Figure 6A). Actin and

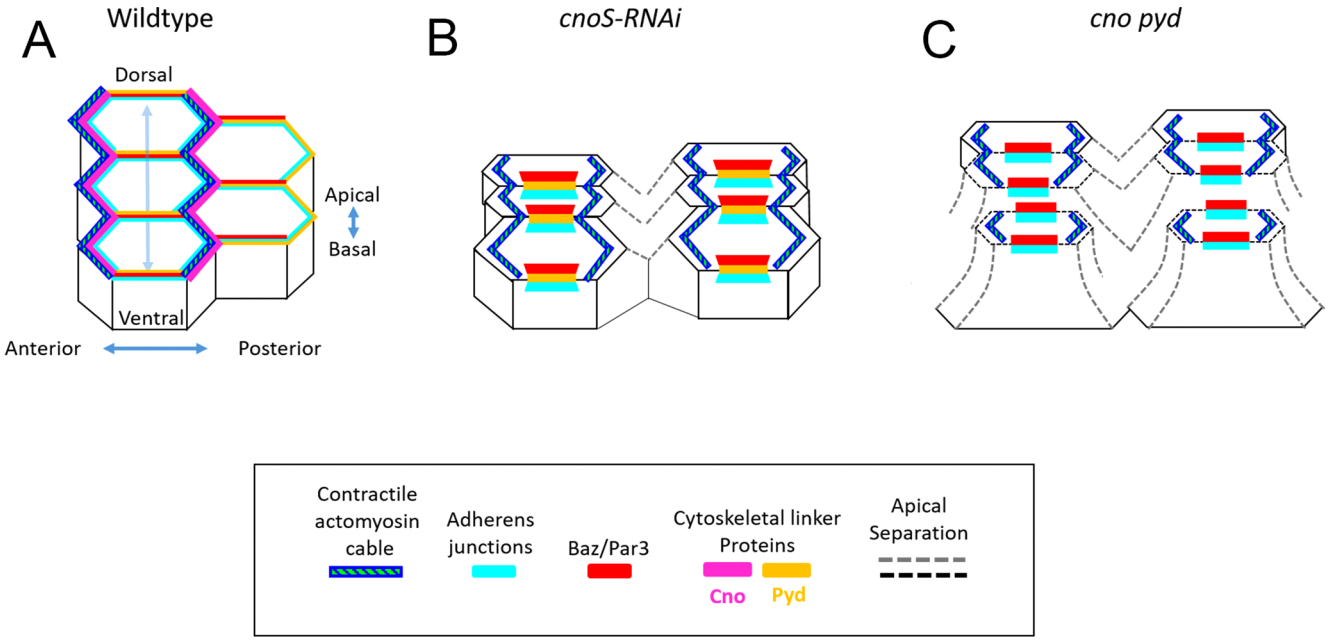

FIGURE 6: Cno and Pyd act together or in parallel to maintain cytoskeletal–AJ linkage and epithelial integrity. Diagram illustrating planar polarization in wild type and *cnoS-RNAi* and *pyd cno* mutants, respectively, during cell intercalation as the germband extends. In wild type, contractile actomyosin cables (green and blue stripes) and Cno (magenta) are slightly enriched at AP borders. Concurrently, AJ proteins (cyan), Pyd (gold), and especially Baz (red) are enriched at DV borders. Cno loss (*cnoS-RNAi*) leads to planar–polarized detachment of the apical actomyosin network while AJ proteins, Baz, and Pyd planar polarity become substantially enhanced and junctions fragmented at DV borders. In a subset of ectodermal cells, there is apical separation (gray dotted lines) of cells across AP borders. In *pyd cno* mutants, gaps (gray dotted lines) at multicellular junctions occur in early gastrulation. Cortical myosin levels are elevated at the AP borders and AJ proteins and Baz planar polarity are further accentuated. By late stage 10, *pyd* cno mutants have wide spread disruptions in epithelial integrity (black and gray dotted lines) at both the AP and DV borders. Cells also become hyper constricted at the apical surface creating breaks and holes along the entire epithelium.

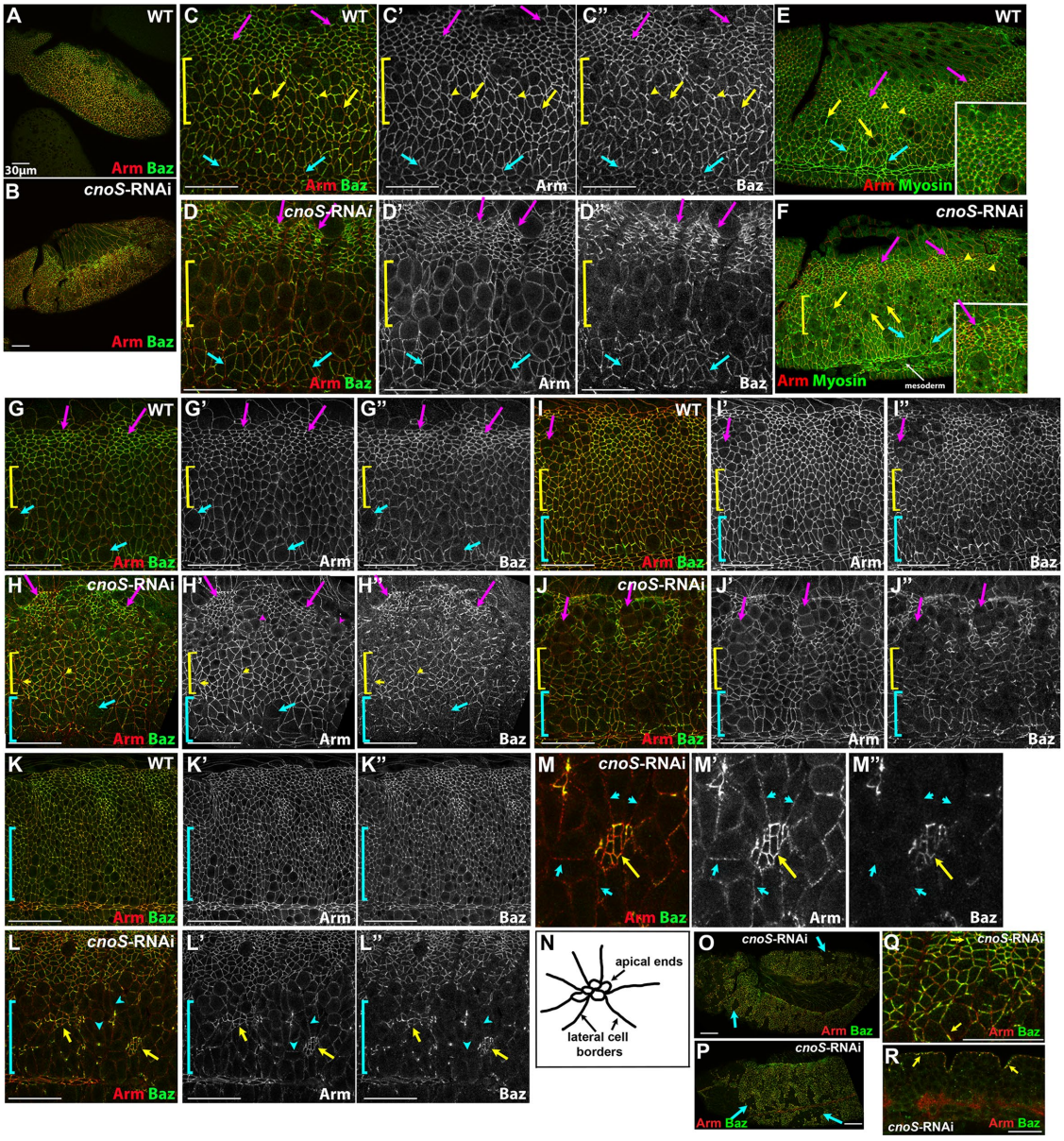

FIGURE 7: Cno is critical for cells to retain columnar architecture when challenged by cell division and neuroblast invagination. Wild-type and *cnoS-RNAi* embryos, genotypes and antigens indicated. (A–F) Stage 9 embryos. A, C, E, wild type. Dorsal ectodermal cells (magenta arrows) have competed their first mitotic divisions and resumed columnar architecture and are apically constricted. The bright myosin dots in these cells, E, are midbody remnants of their first mitotic division. Dorsal neurectoderm cells (mitotic domain N) round up individually for mitosis (C, yellow arrows), with reduced cortical Arm and especially Baz, and then resume columnar architecture rapidly (C, yellow arrowheads). Myosin marks contractile rings of dividing cells (E, yellow arrows). Ventral neurectoderm cells (blue arrows), which have not yet divided, have intermediate levels of Baz relative to their more dorsal neighbors. B, D, F, *cnoS-RNAi*. Dorsal ectodermal cells (magenta arrows) are apically constricted but retain the strongly enhanced planar polarity of Baz. All dorsal neurectoderm cells remain rounded up (D, F, yellow brackets), even though only a subset are still in mitosis, as indicated by myosin marking contractile rings (F, yellow arrow). Ventral neuroectoderm cells (blue arrows) resemble wild type. (G, H) Early stage 10. (G) In wild type, dorsal ectodermal cells (magenta arrows) remain apically constricted relative to their neighbors. Dorsal neurectoderm cells (yellow bracket) have resumed columnar architecture, while ventral neurectoderm cells (blue arrows; mitotic domain M) have begun to enter mitosis individually. (H) In *cnoS-RNAi* embryos, Baz localization is strongly reduced in both dorsal ectodermal cells, especially those that remain rounded up (magenta arrows and arrowheads), as well as in the ventral neuroectoderm (blue bracket, arrows). While the dorsal neuroectoderm is less affected (yellow bracket), Baz localization is less continuous and some cells have formed rosettes (yellow arrowheads). (I, J) Late stage 10. (I) In wild type, a subset of dorsal ectodermal cells have entered mitosis 15 (e.g., magenta arrows), and ventral neuroectoderm cells (blue arrows; mitotic domain M) continue to divide. (J) In *cnoS-RNAi* embryos, many more dorsal ectodermal (magenta arrows) and ventral neuroectoderm cells (blue bracket) remain rounded up with reduced cortical Baz. (K, L) Early stage 11. (K) In wild type, occasional cells in the neuroectoderm (blue bracket) continue to divide individually. (L) In more severely affected *cnoS-RNAi* embryos, most cells in the neuroectoderm have lost columnar shape (blue bracket). Islands of cells remain columnar (yellow arrows). These cells are

myosin are enriched on anterior–posterior (AP) borders, while the cadherin–atenin complex and especially Bazooka (Baz; the fly Par3) are subtly enriched on dorsal–ventral (DV) borders (Supplemental Figure 4, G, yellow vs. blue arrows, quantified in I and J; Figure 6A). In *cnoS-RNAi* embryos, this planar polarity was accentuated, with most of the ectoderm hyperplanar-polarized and cells arrayed in rows along the DV axis (Supplemental Figure 4B; Figure 6B). Arm and Baz planar polarity were substantially enhanced (Supplemental Figure 4, H, blue vs. yellow arrows, quantified in I and J), with reduction in their levels and apical cell separation along AP borders (Supplemental Figure 4H, yellow arrows; Figure 6B), as we observed in *cnoMZ* mutants (Sawyer *et al.*, 2011). Baz localization along DV borders also became more fragmentary rather than continuous. Cortical myosin, which is normally planar-polarized to AP boundaries (Supplemental Figure 4, C and K, inset; Figure 6), pulled away from the AP cell cortex, and cortical levels appeared enhanced (Supplemental Figure 4, D and K, blue arrows vs. K inset; Figure 6B). Separation of myosin from the cortex also occurred at multicellular junctions at the centers of rosettes (Supplemental Figure 4, C and K, yellow arrows)—intriguingly, tricellular and multicellular junctions were also the points most sensitive to Afadin knockdown in ZO knockdown MDCK cells (Choi *et al.*, 2016).

Maintaining integrity of the ectoderm and epidermis requires the cells to maintain epithelial architecture while managing the challenge of the substantial AJ remodeling involved in three processes: cell intercalation during germband elongation, cell rounding during mitosis and the subsequent return to a columnar architecture, and invagination of ~30% of the ectodermal cells as neural stem cells in the neuroectoderm (neuroblasts; NBs). Beginning at the end of stage 7 of embryogenesis, cells across the ectoderm undergo mitosis in programmed groups called mitotic domains (Foe, 1989). As cells enter mitosis, they round up and cortical AJ protein accumulation per unit membrane is reduced (e.g., Supplemental Figure 4E, arrows), as was previously observed in the pupal notum (Pinheiro *et al.*, 2017). NB invagination and the cell rearrangements that drive germband extension overlap with the onset of mitosis of some of the later mitotic domains. This is known to make the ventral epidermis more sensitive to reductions in the function in either junctional or apical polarity proteins (Tepass *et al.*, 1996; Harris and Tepass, 2008). The trunk ectoderm during stage 9 (Figure 7, A and C) can be divided roughly into three regions: 1) the dorsal ectoderm (Figure 7C, magenta arrows), in which the cycle 14 mitoses happen relatively early and from which no NBs delaminate, 2) the more dorsal neuroectoderm (Figure 7C, yellow bracket)—mitotic domain N—in which individual cells divide (Figure 7C, yellow arrows) during embryonic stage 9, and 3) the more ventral neuroectoderm (Figure 7C, blue arrows)—mitotic domain M—in which cells divide during embryonic stage 10. In mitotic domains N and M, cells round up and undergo mitosis individually rather than collectively (Figure 7C, yellow arrows), and this occurs while a subset of the cells invaginate to become neuroblasts (Figure 7C, arrowheads). Mitotic cells then rapidly resume a columnar shape, and thus only a subset of cells are rounded up at any given time. During this process, the apical ends of adjacent dorsal epidermal cells become smaller (Figure 7C, magenta arrows), potentially because their apical contractility is less restrained by their ventral neighbors.

In *cnoS-RNAi* embryos early mitotic domains appeared to fire roughly on schedule at stages 7 and 8 (Supplemental Figure 4, F vs. E), and reduction in cortical AJ proteins appeared similar to that in wild type (Supplemental Figure 4L). However, as germband extension continued and cells in the neuroectoderm initiated mitosis, *cnoS-RNAi* embryos deviated dramatically from wild type (Figure 7, B vs. A). Virtually all cells in the dorsal neuroectoderm (mitotic domain N) were simultaneously rounded up, with reduced cortical cadherin (Figure 7D, bracket), suggesting that they are slower to resume columnar cell shape. Dorsal ectodermal cells became even more highly apically constricted (Figure 7D, magenta arrows) than their wild-type counterparts (e.g., Figure 7C), potentially reflecting reduced contractility in their rounded-up ventral neighbors. Dorsal ectodermal cells also formed clear rows along the AP axis. At stage 9, cells of the ventral neuroectoderm, which have not yet undergone mitosis, were more similar to their wildtype counterparts (Figure 7, D vs. C, blue arrows). Myosin staining highlighted the same differences. In wildtype, cells in the dorsal ectoderm (Figure 7E, magenta arrows) had completed division, with myosin dots marking the remnant midbody (Figure 7E, arrowheads). Mitotic cells in the dorsal neuroectoderm could be identified by their cleavage furrows (Figure 7E, yellow arrows, while ventral neuroectoderm cells retain planar polarized cortical myosin (Figure 7E, blue arrows). In *cnoS-RNAi* embryos, while dorsal ectodermal cells had completed mitosis, as indicated by remnant midbodies (Figure 7F, arrowheads), rows of hyperplanar polarized cells were separated and had elevated cortical myosin (Figure 7F, magenta arrows). While some rounded-up cells in the dorsal neuroectoderm were actively dividing, as indicated by their cleavage furrows, others had completed division, as indicated by the mid-body staining, but not resumed columnar architecture (Figure 7F, yellow arrows). In contrast, the ventral neuroectoderm (Figure 7F, blue arrows) remained relatively normal.

These differences continued and became accentuated during stage 10. In the wild type, cells in the dorsal neuroectoderm resumed a columnar architecture (Figure 7G, bracket), while cells in the ventral neuroectoderm (mitotic domain M) entered mitosis individually (Figure 7G, blue arrows). Slightly later, some cells began their 15th round of mitosis (e.g., Figure 7I, magenta arrow). In contrast, in *cnoS-RNAi* embryos, most cells in the ventral neuroectoderm and some in the dorsal neuroectoderm remain rounded up with reduced cortical Armadillo (Arm; *Drosophila* β-catenin; Figure 7, H and J, blue bracket and arrows). Cells entering mitosis 15 seemed also to be delayed in resuming columnar shape (Figure 7J, magenta arrows). Cell separation was observed at multicellular junctions, suggesting that they are weak points in a relatively intact epithelium (Figure 7I, yellow arrows). As *cnoS-RNAi* embryos entered stage 11, the delay in the resumption of columnar shape in the neuroectoderm was followed by a loss of epithelial integrity, particularly along the ventral midline (Figure 7, L vs. K, brackets). These epithelial disruptions remained through the end of germband retraction and dorsal closure (Figure 7, O and P, arrows) and likely

apically constricted and retain elevated cortical Arm and Baz. They appear to form rosettes with lateral cell borders (blue arrowheads) pointing toward the constricted apices. (M) Close-up of an "epithelial island" in L. (N) Diagram illustrating our interpretation of the "epithelial islands." (O–R) Stage 11, O, Q, or stage 13, P, *cnoS-RNAi* embryos highlighting epithelial holes (blue arrows) and unevenness of Baz accumulation, even in regions where the epidermis remains columnar (Q, yellow arrows). (R) Cross-section through the epidermis of a stage 13 embryo. Baz and Arm remain apically polarized (arrows). Scale bars = 30 μm.

led to the holes in the ventral cuticle we observed. These data suggest a likely role for Cno in reestablishment of columnar epithelial architecture after the challenges posed by mitosis, NB invagination, and cell intercalation.

During establishment of apical–basal polarity, Cno regulates apical positioning of both AJs and the apical polarity determinant Baz during cellularization (Choi *et al.*, 2013), and *cno* mutants have accentuated planar polarity of Ecad and especially Baz during germband extension (Sawyer *et al.*, 2011). Baz plays a key role in maintaining epithelial integrity (Müller and Wieschaus, 1996). We thus examined the effects of Cno knockdown on Baz localization in the ectoderm when cells were challenged by NB invagination and mitotic divisions. In the wild type, Baz localization largely parallels that of Arm (Figure 6). Both Arm and Baz are reduced in cortical intensity in cells rounded up for division, though the reduction is somewhat more pronounced for Baz (Figure 7C", yellow arrows). In contrast, by stage 9, *cnoS-RNAi* has much more severe consequences for Baz localization. In the apically constricted cells of the dorsal ectoderm, Baz remains exceptionally planar polarized, being essentially restricted to DV cell borders (Figure 7D", magenta arrows; Figure 6B). In the rounded-up cells of the dorsal neuroectoderm, Baz is almost completely lost from the cell cortex (Figure 7D", yellow bracket). These differences from the wild type become even more accentuated in stage 10. In rounded-up cells of the neuroectoderm (Figure 7H, blue bracket) and dorsal ectoderm (Figure 7H, magenta arrows), Baz levels are reduced even more than those of Arm, while Baz levels remain high in the hypercontracted dorsal ectodermal cells (Figure 7H", magenta arrows). Even in less disrupted regions of the epidermis, Baz and to a lesser extent Arm localization became more uneven, with some cell borders having much higher levels than others (Figure 7Q, arrows), although the overall apical–basal polarization of Arm and Baz remains relatively normal (Figure 7R).

By stage 11, epithelial architecture is lost in the ventral neuroectoderm, with small "islands" of apically constricted cells seemingly separated from one another (Figure 7, L and M, yellow arrows). We suspect that this reflects a situation where a subset of cell junctions fail, leading to unbalanced apical contractility and allowing groups of cells to constrict apically when they were released from the contractile restraint of their neighbors. The bright islands of Arm and Baz staining would thus be the constricted apical ends of these cell groups, while the adjacent regions that stain for Arm and not Baz represent the lateral borders of the apically constructed cells in the island (Figure 7, L and M, blue arrowheads; diagrammed in N). This would parallel what we observed in Afadin ZO knockdown MDCK cells, with some cell junctions failing and a subset of cell borders hyperconstricted while others were hyperextended (Choi *et al.*, 2016). Together, these data suggest that Cno plays an important role in allowing cells to maintain epithelial integrity when challenged by junctional remodeling during morphogenetic movements, and that the polarity protein Baz is most sensitive to Cno loss. However, they also reveal that many cells can maintain columnar epithelial architecture even when Cno is lost, in contrast to cells lacking Baz or core AJ proteins.

Pyd/ZO-1 works in parallel with Canoe to maintain epithelial integrity

Afadin, Cno's mammalian homologue, acts in parallel with ZO-1 family proteins to maintain epithelial integrity in cultured mammalian cells (Choi *et al.*, 2016). In *Drosophila*, unlike mammals, both Cno and Pyd localize to AJs (Takahashi *et al.*, 1998; Wei and Ellis, 2001; Jung *et al.*, 2006; Seppa *et al.*, 2008; Sawyer *et al.*, 2009; Choi *et al.*, 2011). Strikingly, Pyd localization mirrors that of the AJ proteins even in the one place where Cno and AJ proteins differ subtly. During germband extension, Baz and AJ proteins are subtly enriched on DV cell borders (Zallen and Wieschaus, 2004; Blankenship *et al.*, 2006; Harris and Peifer, 2007); this is more apparent for Baz, whose planar polarization is more pronounced (Supplemental Figure 5A", yellow vs. blue arrows; Figure 6A). At this stage, we found that Pyd localizes like the other AJ proteins (Supplemental Figure 5, A'" vs. A'; Figure 6A). In contrast, Cno is enriched on AP cell borders (Sawyer *et al.*, 2011), like myosin and actin (Bertet *et al.*, 2004; Zallen and Wieschaus, 2004). Loss of Cno enhances the planar polarity of Arm and Baz, by reducing their levels on AP cell borders (Sawyer *et al.*, 2011; Supplemental Figure 5, B and B", yellow vs. blue arrows; Figure 6B) and in parallel enhances the planar polarity of Pyd (Supplemental Figure 5B"', yellow vs. blue arrows; quantified in Supplemental Figure 5C; Figure 6B). However, Cno loss does not dramatically alter levels of cortical Pyd (Supplemental Figure 5, B vs. A, E vs. D; Sawyer *et al.*, 2009).

Cno and the ZO-1 homologue Pyd interact both physically and genetically (Takahashi *et al.*, 1998), supporting the idea that they might act together or in parallel. However, previous studies of genetic interactions were confined to partially functional alleles. To determine whether and how Cno and Pyd acted in parallel, we sought to combine strong reduction of both. The close proximity of the two genes in the genome precluded combining null alleles of both on the same chromosome by recombination. We chose a different approach, combining complete maternal and zygotic loss of Pyd (Choi *et al.*, 2011) with strong (though not complete) maternal and zygotic reduction of Cno via RNAi (*matGAL4/+; cnov20shRNA pyd/pyd* females × *cnov20shRNA pyd/+* males; heterozygous males were chosen due to the semisterility of *pyd* homozygous males; crosses and resulting progeny are diagrammed in Supplemental Figure 3). We can distinguish by immunofluorescence analysis the 50% that are maternally *and* zygotically *pyd* mutants by their lack of Pyd staining, and the strongest 25% of the embryos will also have two zygotic copies of the *cnov20shRNA* (*cnov20shRNA pyd/ cnov20shRNA pyd*—referred to as *pyd cno* double mutants below). As a control for Cno reduction alone, we compared our double mutants with embryos with the same degree of Cno reduction but retaining wild-type levels of Pyd (*matGAL4/+; cnov20shRNA/+* females × *cnov20shRNA/+* males). Cell biological analysis revealed that the more severe embryos from this control cross (likely those receiving two copies of the *cnov20shRNA* zygotically) were similar in phenotype to those of *cnoS-RNAi* embryos (Supplemental Figure 6). We also compared the phenotype of double mutants with our strongest *cno* RNAi (*cnoS-RNAi*, the genotype analyzed above), which immunoblotting (Supplemental Figure 1) and cuticle analysis (Figure 1) suggest phenocopy complete loss of Cno.

To confirm the genotypes and assess the degree of Cno knockdown, we performed immunoblotting. The combination of GAL4 driver and *cnov20shRNA* used in our control cross produced nearly complete knockdown of maternal Cno, as assessed in 1–4 h–old embryos (3.6% of wild type; Supplemental Figure 1, D and E). Knockdown remain strong but not complete at 12–15 h (8.1% of wild type; Supplemental Figure 1, D and F)—due to variability in the number of *cnov20shRNA* copies they receive, late Cno knockdown likely varies among embryos. Embryos from the *pyd cno* cross had similar levels of Cno knockdown (2.7% of wild type at 1–4 h and 6.5% of wild type at 12–15 h; Supplemental Figure 1, D–F; we also verified knockdown by immunofluorescence; Supplemental Figure 1, J vs. I). Our analysis also verified the strong reduction of Pyd in this population (Supplemental Figure 1, D–F)—the remaining Pyd

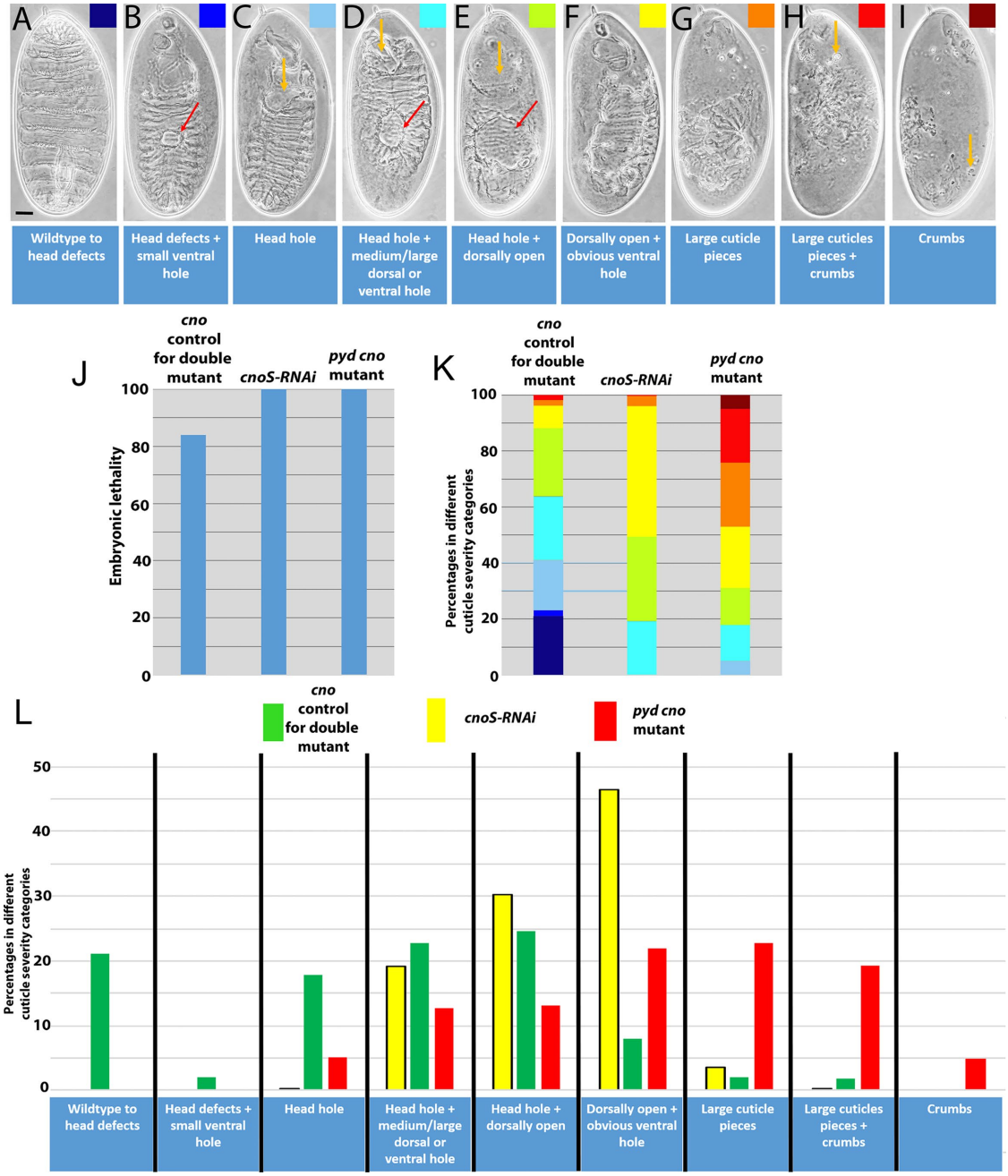

FIGURE 8: Loss of Pyd substantially enhances the effects of Cno loss on morphogenesis and epithelial integrity. (A–I) Cuticle preparations revealing the spectrum of defects in morphogenesis and epithelial integrity seen in *cnoS-RNAi, pyd cno,* and *cno control* knockdown embryos, as in Figure 1. Scale bar, 30 µm. (J) Embryonic lethality. (K, L) Two illustrations of the enhancement of the severity of the Cno knockdown cuticle phenotype by loss of Pyd. *pyd cno* mutants have defects that are much more severe than the corresponding *cno RNAi control* and that are even more severe than those of *cnoS-RNAi.*

seen in 1–4 h embryos and the partial return of Pyd at 12–15 h reflect the 50% of embryos that are zygotically rescued. We also examined effects on accumulation of the AJ protein Arm. Arm levels were essentially unchanged at 1–4 h and somewhat reduced at 12–15 h (Supplemental Figure 1), consistent with our earlier analysis of *cnoMZ* mutants (Sawyer *et al.*, 2009).

As an initial analysis of the effects of reducing both Pyd and Cno on morphogenesis, we examined effects on morphogenesis and epithelial integrity by analyzing embryonic lethality and cuticle patterning. The Cno knockdown cross that serves as the control for our double mutant (cross and progeny diagrammed in Supplemental Figure 3) led to partially penetrant embryonic lethality (84% lethality, $n = 696$; Figure 8J). Among the lethal embryos, many had a wild-type or only mildly defective cuticle (21%; Figure 8, A–I and K, and Table 1; these embryos and those that are embryonically viable are likely the 25% carrying no zygotic copy of the *cno20shRNA* construct). Most of the rest had significant defects in head involution and dorsal closure, with the most severe also having holes in the ventral epidermis (roughly 10%; Figure 8K and Table 1). Pyd loss alone has milder effects, even in maternal zygotic null mutants, with 60% embryonic

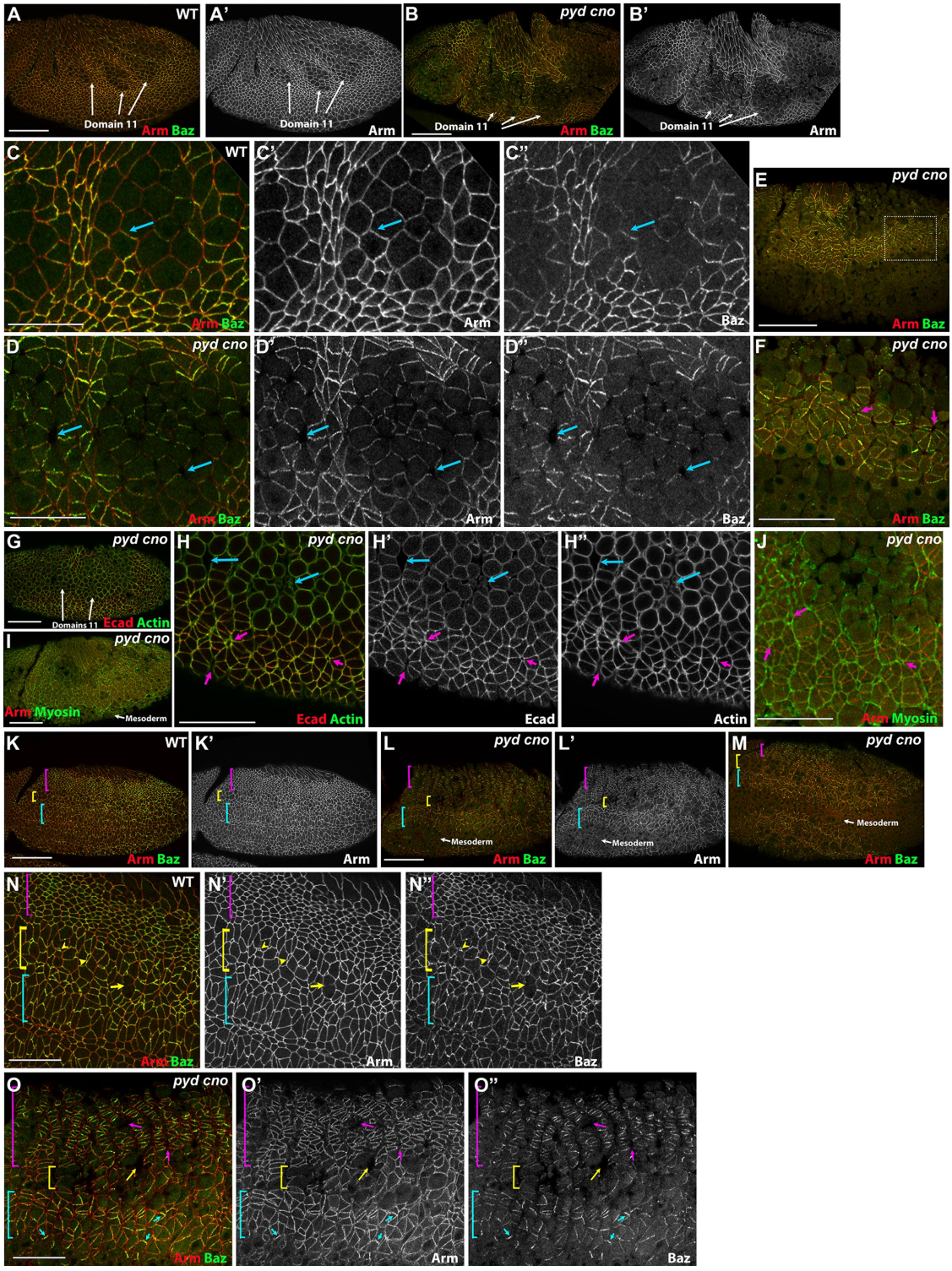

FIGURE 9: Loss of epithelial integrity begins earlier in *pyd cno* double mutants and Baz localization is affected earlier than that of AJs. (A–J) Stage 8 embryos focused on early mitotic domain 11. (A, B) This mitotic domain fires on time in *pyd cno* mutants. (A–D) Cortical Arm and Baz accumulation are reduced in dividing cells in both wild type (A, C, arrows) and *pyd cno* (B, D, arrows). However, in *pyd cno* mutants large gaps appear between dividing cells (D, arrows) that are not seen in wild type. (E, F) In *pyd cno* mutants, in more ventral cells that have yet to divide, both Arm and Baz become hyperplanar-polarized, and gaps appear at multicellular junctions where cells are forming rosettes (F, arrows). Dotted box in E indicates area enlarged in F. (G, H) In *pyd cno* mutants staining with Ecad and actin also highlights large gaps between dividing cells in mitotic domain 11 (H, blue arrows) and gaps at the center of rosettes more ventrally (H, magenta arrows). (I, J) In *pyd cno* mutants, cortical myosin is elevated at anterior–posterior boundaries and often separates from the cortex, particularly at tricellular and multicellular junctions (J, magenta arrows). (K–O) Stage 9 embryos. (K, N) In wild type, dorsal ectodermal cells (magenta brackets) have completed their first division, apically

lethality and only mild defects in head involution and dorsal closure in the nonviable embryos (Choi *et al.*, 2011). In contrast, embryos from the *pyd cno* double mutant cross were 100% lethal ($n = 374$; Figure 8J) and exhibited much more severe defects in morphogenesis and epithelial integrity (Figure 8, K and L; Table 1). In addition to complete failure of head involution and dorsal closure, 69% had defects in epidermal integrity. Most strikingly, 24% had only pieces of intact cuticle remaining, a fraction equivalent to the quarter of the progeny that were both *pyd* maternal and zygotic mutant and had the strongest *cno* knockdown. Importantly, the defects of those embryos were significantly more severe than those of *cnoS-RNAi* embryos (Figure 8, K and L; Table 1), which have essentially complete *cno* maternal/zygotic knockdown (Supplemental Figure 1). These data suggest that Cno and Pyd act in parallel to ensure epithelial integrity.

pyd cno mutants exhibit defects in epithelial integrity from the onset of gastrulation, and tricellular and multicellular junctions are the weakest points

We thus explored the cell biological basis of these strong defects in epithelial integrity. While the *pyd cno* cross produces embryos of four genotypes (Supplemental Figure 3), by staining embryos with Pyd antibody we could focus on the half that were *pyd* maternal/zygotic mutant, thus lacking Pyd staining. All had equivalent maternal Cno knockdown, and they varied in the amount of zygotic Cno knockdown. Below we refer to these as *pyd cno* mutants. During gastrulation onset, they shared with *cnoMZ* and *cnoS-RNAi* mutants defects in apical positioning of AJs and Baz during cellularization (Supplemental Figure 7A; Choi *et al.*, 2013); defects in mesoderm invagination (Supplemental Figure 7, B and C); strongly accentuated planar polarity of AJs and Baz, which exceeded that seen after *cnoS-RNAi* (Supplemental Figure 7, C and C inset, magenta arrows; Figure 6; quantified in Supplemental Figure 4, I and J); and enhancement of cortical myosin along with myosin disconnection from cell junctions at AP cell borders as germband extension initiated (Supplemental Figure 7, D and E). The hyperplanar polarization of Baz and Arm at DV borders and myosin at AP borders, as well as cell alignment into rows (Supplemental Figure 7C inset, yellow arrows) were further accentuated relative to *cnoS-RNAi* embryos, with grooves appearing along the AP axis between adjacent rows of cells (Supplemental Figure 7C inset, blue arrows). Two particularly deep grooves appeared to coincide with the positions of the normally transient dorsal folds (Supplemental Figure 7C, yellow arrows). The first mitotic domains, including mitotic domain 11 in the trunk, fired in a timely manner (Figure 9, A and C vs. B and D, white arrows), but cortical Arm in dividing cells was less continuous and large gaps appeared at multicellular junctions between some rounded-up cells (Figures 9, C vs. D, blue arrows, and 6). In *pyd cno* mutants, adjacent nondividing cells in the neuroectoderm formed rosettes with gaps in the center at multicellular junctions (Figure 9, E and F, magenta arrows). F-actin staining also highlighted the gaps at tricellular/multicellular junctions between dividing cells (Figures 9, G and H, blue arrows, and 6C) and at the centers of rosettes of nondividing cells at multicellular junctions (Figure 9H, magenta arrows). In *pyd cno* mutants, cortical myosin levels were highly elevated at AP cell borders (Figures 9, I and J, and 6C) and myosin separated from the cortex at many vertices (Figures 9J, arrows, and 6C). These data suggest that *pyd cno* mutants are even more sensitive to the stresses of rounding up for division and of cell rearrangements during germband extension, that tricellular and multicellular junctions are the weakest points, and that loss of both Pyd and Cno strongly accentuates the reciprocal planar polarity of Baz/Arm versus myosin.

pyd cno mutants exhibit loss of cortical Bazooka localization preceding widespread loss of epithelial integrity

pyd cno mutants roughly resembled *cnoS-RNAi* embryos as cells in the dorsal neuroectoderm (mitotic domain N) began to round up for division (Figure 9, K vs. L, M vs. Figure 7D), possessing hyperconstricted dorsal ectoderm cells arrayed in rows (Figure 9, N vs. O, magenta brackets) and virtually all cells in the dorsal neuroectoderm rounded up (Figure 9, N vs. O, yellow brackets). However, the ectoderm was more significantly disrupted than in *cnoS-RNAi*. As cells separated apically, grooves along the AP axis between rows of dorsal ectodermal cells were further accentuated and holes appeared (Figure 9O, magenta arrows). Large gaps appeared between dividing cells in the dorsal neuroectoderm (Figure 9O, yellow arrow). In the ventral neuroectoderm (Figure 9, N vs. O, blue brackets), junctional accumulation of Baz became widely fragmented in *pyd cno* mutants (Figure 9O, blue arrows; 38% of *pyd cno* mutants have these stronger phenotypes at stage 9, $n = 19$), in contrast to the more intact Baz staining seen in *cnoS-RNAi* embryos (Figure 7D). Thus, loss of Pyd continued to strongly enhance the effects on epithelial integrity of Cno knockdown.

As embryos proceeded into stage 10, loss of epithelial integrity in *pyd* cno mutants became even more widespread (Figure 10, A vs. B, C), ranging from embryos at the most severe end of the phenotypes seen in *cno*S-RNAi embryos (Figure 10B) to those with global disruption of the epidermis (Figure 10C). At this stage in the wild type, most cells across the epidermis have resumed a columnar architecture (Figure 10D), with small groups of cells or individual cells in mitosis 15 (Figure 10D, arrow). In contrast, in most *pyd cno* mutants (55% of *pyd cno* mutants at stage 10; $n = 50$), cells of the neuroectoderm formed into separate balls (Figure 10E, white arrows) segregating from their neighbors, and as a result the surface of the embryo became highly irregular. In these regions, AJ proteins and Baz staining became highly fragmented (Figure 10E, blue arrows), with only small groups of cells retaining cortical Arm. As we saw at stage 9, junctional accumulation of Baz was much more strongly affected than that of Arm (Figure 10E, yellow and magenta arrows). Strikingly, the amnioserosa was much less affected (Figure 10, B and C, red arrows).

In *pyd cno* mutants, unbalanced contractility was even more pronounced than after *cno*S-*RNAi,* as groups of cells separated from their neighbors. The enhanced apical constriction of dorsal ectodermal cells led to the folding of these cells inward at the junction with the amnioserosa (Figure 10, F and F inset). Meanwhile,

constricted, and resumed columnar shape. Some cells of the dorsal neuroectoderm (yellow brackets) are individually dividing (N, yellow arrow), while others invaginate as neuroblasts (N, yellow arrowheads). Cells of the ventral neuroectoderm (blue brackets) have yet to divide. (L, M ,O) *pyd cno* mutants. Dorsal ectoderm cells (magenta brackets) form prominent rows along the dorsal ventral axis, with hyperplanar-polarized Arm and Baz. Gaps appear between many of the rows (O, magenta arrows). Dividing cells of the dorsal neuroectoderm (yellow brackets) have reduced Arm and Baz staining and gaps appear between cells (O, yellow arrow). In the ventral neuroectoderm (blue brackets), while Arm cortical accumulation remains largely intact, Baz cortical localization has become fragmented, with only some cell borders retaining Baz (O, blue arrows). Scale bars in A, B, E, G, I, K, and L = 20 μm. All other scale bars = 10 μm.

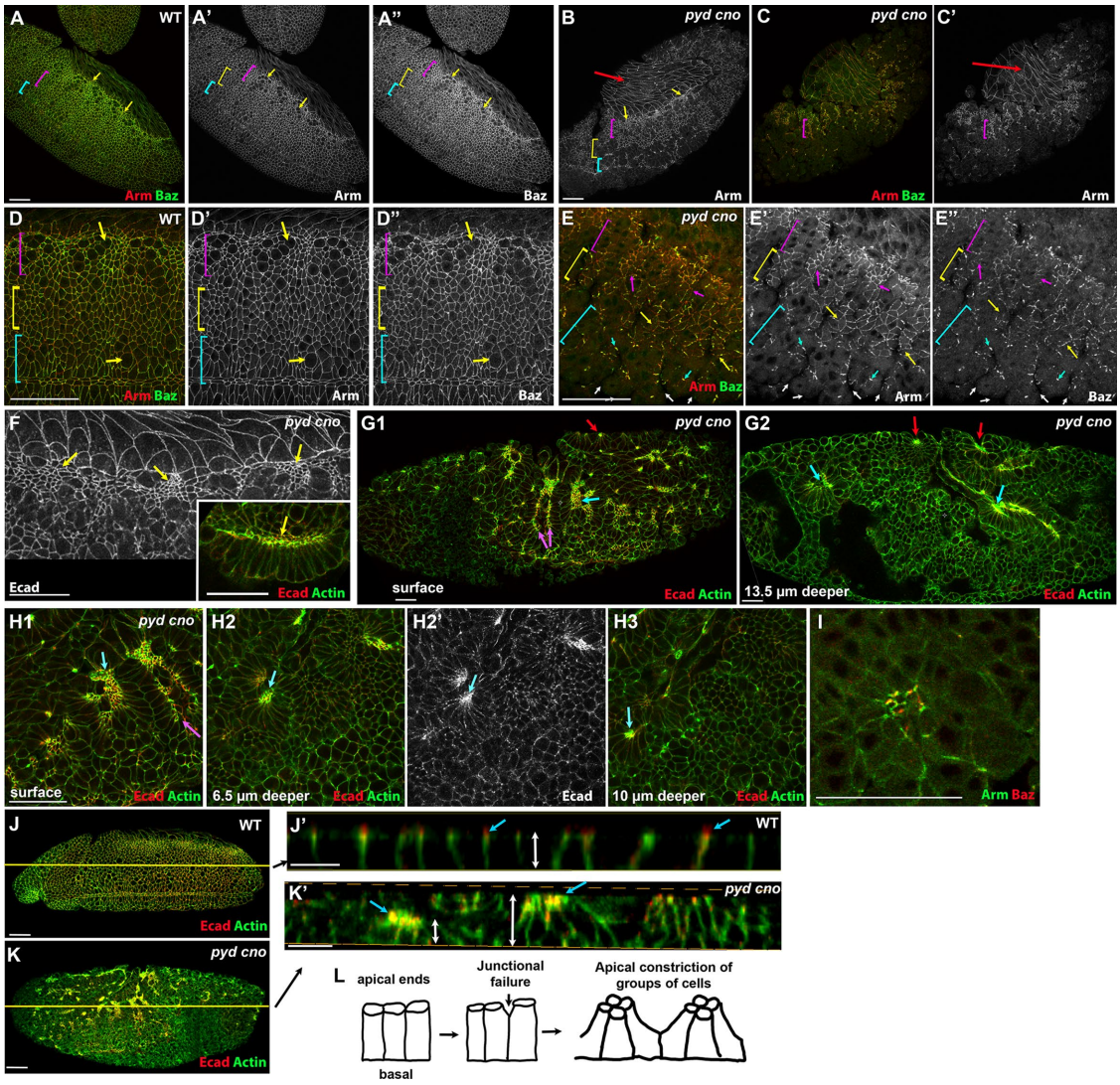

FIGURE 10: In *pyd cno* mutants, epidermal integrity is rapidly lost as cells separate into epithelial islands and balls. (A–E) Late stage 9/early stage 10 embryos. (A, D) Wild type. Dorsal ectoderm cells (D, magenta bracket) are generally columnar and apically constricted with a few entering mitosis 15 (D, top arrow). Dorsal neuroectoderm cells (yellow bracket) have largely completed division and resumed columnar architecture. Individual cells of the ventral neuroectoderm (blue bracket) continue to divide (D, bottom arrow). (B, C, E) In *pyd cno* mutants, epidermal integrity is rapidly lost. (B) Less severe example. Dorsal ectoderm (arrows) and some dorsal neurectoderm cells (magenta bracket) remain epithelial while only small epithelial islands remain in the ventral neuroectoderm (blue bracket). (C, E) More severely affected embryo. At the surface, only small groups of cells in the dorsal ectoderm (E, magenta arrows) and dorsal neuroectoderm (E, yellow arrows) remain epithelial, and even in these cells, cortical Arm localization is more intact than is Baz. In the ventral neuroectoderm, only junctional fragments remain (E, blue arrows). (F, F inset) In less severely affected *pyd cno* embryos, dorsal ectodermal cells become highly apically constricted (arrows). This often results in groups of ectodermal cells at the border of the amnioserosa folding inward, with their apical ends turned ventrally (inset). (G, H) Widespread loss of epithelial integrity in *pyd cno* mutants fragments the embryo into groups of cells that remain associated with one another, but have lost junctional contact with other neighbors. Groups of cells fold inward to form epithelial folds and balls. This is readily seen by taking different sections through an embryo. (G1, H1) Surface views. Only small patches of cells retain columnar architecture, and these have apical ends that are severely apically constricted (blue arrows). Other cells can be seen folding inward as sheets (magenta arrows) or rosettes. (G2, H2, H3) Deeper sections through the embryo reveal other groups of cells that have been internalized as epithelial balls (G2, red arrows), rosettes, or sheets (blue arrows). In these cells, Ecad and actin remain enriched apically. (I) In some epithelial balls Baz can also be observed apically retained. (J, K) Stage 10 embryos. Surface views. Lines indicate plane of section shown in close-ups. (J', K') Cross-sections generated using Imaris. (J') In wild type, cells are even in height (double-headed arrow) and columnar in architecture and have Ecad enriched at the apical junctions (blue arrows). (K') In *pyd cno* mutants, the embryo surface becomes very uneven, with cells varying in height (double-headed arrows). Ecad and actin remain enriched at apical ends of groups of apically constricted cells (blue arrows). (L) Diagram illustrating our interpretation of the progression in *pyd cno* mutants. Cells begin columnar (left). A subset of cell junctions fail (middle) and groups of cells then apically constrict (right). Scale bars = 20 µm in panels A–E, G1, and G2. Scale bars = 2 µm in panels J and K. All other scale bars = 10 µm.

small islands of epithelial cells in the neuroectoderm formed epithelial balls and sheets. Many of these became internalized into the embryo, as was revealed by imaging successively deeper sections in the embryo (Figure 10; arrows indicate groups of apically constricted cells). However, in these epithelial cell clusters, Ecad, actin (Figure 10H, arrows), and occasionally Baz (Figure 10I) remained enriched on their apical ends. The 3D nature of these epithelial disruptions was reinforced when we used Imaris to generate 3D renderings of the surfaces of wild-type and mutant embryos (Figure 10, J and K). Cross-section slices through wild-type embryos revealed cells of uniform height and columnar architecture, with apical enrichment of Ecad (Figure 10J'). In contrast, sections through *pyd cno* mutants revealed separate groups of apically constricted cells with variable height (Figure 10K'). These data suggest that in *pyd cno* mutants the junctional remodeling accompanying mitosis and neuroblast invagination imposes stress on adhesion, leading to separation at weaker cell interfaces (diagrammed in Figure 10L). Groups of cells that retain cell adhesion then apically constrict and are internalized as large folds or epithelial balls. Together, these data reveal that Pyd and Cno work in parallel to maintain epithelial integrity when challenged by the junctional remodeling inherent in morphogenesis, and further suggest that they may exert their effects by regulating Baz cortical localization during this process.

DISCUSSION

Linkage of the actomyosin cytoskeleton to cell–cell and cell–matrix junctions drives cell shape change during normal embryonic development and adult homeostasis. One key question for the field involves defining how cell–cell junctions are dynamically regulated to allow cells to move within the plane of the epithelium and change shape without disrupting epithelial integrity. The *Drosophila* embryo provides a superb place to test hypotheses as cells divide, ingress, and undergo the shape changes and cell rearrangements involved in morphogenesis. Here, we explored how the junctional proteins Cno/Afadin and Pyd/ZO-1 act together or in parallel to maintain epithelial integrity.

Cno: more than just a junction:cytoskeletal linker

We initially pursued Cno as a potential core component of the AJ, like Ecad and the catenins. However, loss of Cno does not lead to immediate loss of epithelial architecture; instead, it disrupts a series of cell shape changes requiring linkage of the actomyosin cytoskeleton to AJs (Sawyer *et al.*, 2009, 2011). This led us to hypothesize that Cno acts as one of several proteins that link junctions and the cytoskeleton and that it reinforces these linkages under mechanical tension. Our work on Afadin in mammalian MDCK cells (Choi *et al.*, 2016) suggested a further modification, as loss of Afadin did not uniformly disconnect junctions from the cytoskeleton. Instead, tricellular and multicellular junctions were most sensitive to Afadin loss. Our data suggested that this resulted from those junctions being the site of end-on linkage of bicellular actin cables to cadherin-based junctions, and thus the place with the highest "molecular tension" on junctional proteins. Afadin knockdown disrupted junctional–cytoskeletal linkage at tricellular junctions, and the normally tightly bundled junctional actin and myosin spread broadly across the lateral membrane. These local disruptions could then spread to adjacent bicellular junctions. The MDCK cell data also suggested that reducing Afadin function led to loss of contractile homeostasis, with some cell borders becoming hyperconstricted and others hyperextended. This prompted us to return to the embryo with these insights in mind.

Our current data support and amplify this idea, allowing us to explore both tricellular/multicellular junctions in a single tissue (the ectoderm during and after gastrulation) and those at the interface between two tissues (the lateral epidermis and the amnioserosa during dorsal closure). During dorsal closure, the leading edge (LE) provides an interesting model of balanced contractility. The planar-polarized supercellular actomyosin cable along the LE provides part of the force-generating machinery that powers dorsal closure (reviewed in Hayes and Solon, 2017; Kiehart *et al.*, 2017; though see Ducuing and Vincent, 2016; Pasakarnis *et al.*, 2016). Each border is a separate contractile unit, pulling on its neighbors, but in the wild type each cell's cable is equivalently contractile to its neighbors, maintaining relatively uniform LE cell widths across the cable. Our SIM superresolution imaging builds on earlier work, supporting the idea that the LE actin cable is linked cell–cell at each LE AJ, with Ecad and Cno enriched at LE tricellular junctions, and Ena localization suggesting that actin barbed ends are also enriched at those sites. Myosin is enriched at the medial region of each LE cable. We found that strong reduction of Cno function does not abrogate actin cable assembly at the LE, nor does it block contractility. Instead, LE contractility appears to become unbalanced, with LE cells becoming hyperconstricted or hyperelongated. This occurs in parallel with disruption of actin architecture at the LE, as reflected by loss of focused Ena localization at LE junctions, which may reflect alterations in the localization of actin barbed ends. We speculate that this reflects failure of end-on actin attachment at a subset of LE tricellular junctions. These cells then cannot counter the contractile force of their neighbors, and splay open, while their neighboring cells, released from the resistance of those neighbors, hyperconstrict. These data are quite consistent with the junctional failure at tricellular and multicellular junctions and the unbalanced contractility we observed in MDCK cells after Afadin ZO knockdown (Choi *et al.*, 2016).

The *pyd cno* mutant phenotypes also are interesting when viewed from this perspective. In mutants, cells form rows and rosettes from gastrulation onset, with cell separation and loss of junctional integrity focused at AP cell borders and multicellular junctions. Later, this progresses to more global epithelial disruption. One speculative interpretation of these disruptions is that, as we observed in Afadin/ZO knockdown MDCK cells, junctional integrity and junction–cytoskeletal linkage failure first occurs at tricellular junctions, but spreads more broadly after the initial disruption. This leads to unbalanced contractility between different groups of cells. Cells that retain junctional connections constrict apically, as they are no longer effectively resisted by adjacent cells in which junctional connections have been weakened or lost. Strikingly, in *pyd cno* mutants, these groups of cells sometimes go on to move inward, forming epithelial rows or balls that to secrete the cuticle pieces we observe in the terminal phenotype. One important future direction will be to generate fly lines that allow us to visualize junctional and cytoskeletal proteins live in *cnoS-RNAi* and *pyd cno* mutant backgrounds, allowing us to observe the order of events more directly.

One place where unbalanced contractility is a necessary feature of normal cell rearrangements is germband extension. Wild-type embryos rely on "regulated unbalanced contractility," resulting from the planar polarization of junctional and cytoskeletal proteins (reviewed in Kong *et al.*, 2017). Actin and myosin accumulate at elevated levels on anterior–posterior (AP) borders, while adherens junction proteins and Baz are elevated at dorsal–ventral (DV) borders. In the wildtype these differences are subtle, but they drive constriction of AP borders and thus cell rearrangements. However, adhesion remains robust enough so that this does not lead to disruption of cell adhesion and thus to cell separation. Intriguingly, Cno

is elevated at AP borders, along with actin and myosin, rather than at DV borders with other junctional proteins (Sawyer *et al.*, 2011). We speculated that it may act there to make sure the connection of AJs to the actomyosin cytoskeleton is not disrupted during contractility. In contrast, in *cno* mutants, the planar polarity of AJs and Baz is substantially elevated, due to reduced accumulation at AP borders (Sawyer *et al.*, 2011). Our data here suggest that cortical myosin is elevated on the opposing AP borders. This leads to preferential cell separation at AP borders, where AJ levels are reduced and contractility is elevated. These differences are even more accentuated in *pyd cno* mutations. This fits well into the emerging idea that cell adhesion and cortical actomyosin are inversely correlated, in a balance between adhesion strength and cortical tension (Maitre and Heisenberg, 2011, 2013; Winklbauer, 2015). Thus, one might speculate that the reduction in adhesion at a particular cell border in *cno* or *pyd cno* mutants might lead to elevated actomyosin contractility, which might in turn further reduce adhesion. This kind of runaway feedback process might explain why adhesion fails at a subset of cell borders, leading to cell separation and the formation of cell groups and epithelial balls.

Recent work has suggested that tissues can undergo "solid-to-liquid" transitions, allowing cell rearrangements and thus driving morphogenetic events such as *Drosophila* germband elongation (e.g., Tetley and Mao, 2018; Yan and Bi, 2019). This event involves modulation of both cytoskeletal contractility and cell adhesion. At the molecular level, this must involve changes in the interactions between AJs and the cytoskeleton, with these connections made less rigid. Further, it often must occur in a planar-polarized manner. As noted above, Cno loss perturbs germband elongation and enhances the planar polarization of AJs and Baz, and our current work reveals that this becomes even more exaggerated in *pyd cno* mutants. Perhaps Cno and Pyd act to limit the solid-to-liquid transition, thus protecting tissue integrity. It would be intriguing to include them in future mathematical modeling of this process.

Another overlapping question involves the mechanisms acting upstream of Cno. In most tissues examined, the small GTPase Rap1 regulates Cno localization and function (Knox and Brown, 2002; Boettner *et al.*, 2003; Sawyer *et al.*, 2009, Bonello *et al.* 2018). It will be fascinating to explore the effects of Rap1 loss on epithelial integrity, which cuticle analysis suggests is affected. Previous analysis of Rap1 function in larval and pupal imaginal discs provides some intriguing clues. Clones of imaginal disc cells mutant for Rap1 have intriguing properties suggesting roles in regulating adhesion and contractility. Normal clones of cells remain as coherent groups; in contrast, clones of cells mutant for Rap1 disperse among their neighbors, suggesting alterations in adhesion. Loss of Rap1 also disrupts the normal hexagonal cell shape, and apical area is increased, consistent with changes in apical contractility (Knox and Brown, 2002; O'Keefe *et al.*, 2009). Most intriguing, Rap1 loss disrupts the normally uniform distribution of Ecad, Cno, and Pyd to different cell borders—in clones of mutant cells some borders accumulate abnormally elevated levels of Ecad, Cno, and Pyd while other borders have lower than normal levels (Knox and Brown, 2002). This is strikingly similar to the effects on AJ and especially the Baz accumulation we saw in *cnoSRNAi* and *pyd cno* mutant embryos. Wing imaginal discs also provide another place where "regulated unbalanced contractility" and "liquid/solid transitions" come into play. In cells of the wing vein, epidermal growth factor receptor signaling shapes the fate and behavior of the rows of cells that develop into wing veins. These cells become planar-polarized, with elevated Ecad and reduced Cno accumulation at vein:vein borders, and rectangular rather than hexagonal shapes. Both of these properties are regulated by Rap1, with data suggesting epidermal growth factor receptor signaling turns down Rap1 activity (O'Keefe *et al.*, 2012). It will be fascinating to explore the role of Rap1 in the embryonic ectoderm and to identify its upstream regulators.

When speculating about mechanism, it is useful to note what does and does not go wrong after Cno loss or in *pyd cno* mutants. Even in severely disrupted regions of the embryo, cells that retain junctional connections also retain epithelial polarity, as reflected by continued apical junctional enrichment of Ecad, Arm, and Baz and the apical enrichment of actin. However, our data also support the idea that Baz is the weak link in maintaining epithelial integrity. In *pyd cno* mutants, disruption of Baz localization is much more dramatic than effects on core AJ proteins. It is lost earlier in regions in which junctional remodeling is occurring and Baz localization became less uniform even in regions of the epidermis that remain intact.

Baz/Par3 has an interesting and complex relationship with myosin. During germband extension Baz and myosin have opposing planar polarization (Zallen and Wieschaus, 2004; reviewed in Kong *et al.*, 2017), with activation of Rho kinase and Abelson tyrosine kinase (Abl) on AP borders working in parallel to simultaneously activate myosin and down-regulate cortical localization of AJ proteins and Baz, respectively (Simoes Sde *et al.*, 2010; Tamada *et al.*, 2012). The tension generated by myosin contractility reinforces these opposing polarities (Fernandez-Gonzalez *et al.*, 2009; Fernandez-Gonzalez and Zallen, 2009; Levayer *et al.*, 2011). However, during mesoderm apical constriction, tension generated by apical myosin contractility can also strengthen AJs (Weng and Wieschaus, 2016, 2017), suggesting that the circuitry connecting adhesion and myosin-driven contractility is complex and context dependent. In one-cell *Caenorhabditis elegans* embryos Par3 and myosin have a similarly complex relationship. Par3 and contractile myosin foci both are found in the anterior domain, but they are interspersed rather than colocalizing. Par proteins regulate myosin contractility (Cheeks *et al.*, 2004; Munro *et al.*, 2004), while cortical myosin flow and contractility regulate Par protein polarization and clustering (Dickinson *et al.*, 2017; Rodriguez *et al.*, 2017; Wang *et al.*, 2017). Our data are especially intriguing given that the known role of Baz as a regulator of apicomedial actomyosin contractility in the *Drosophila* amnioserosa, where it regulates pulsatile contractions and the degree of coupling to cell shape change, via effects on atypical protein kinase C (aPKC; David *et al.*, 2010; Durney *et al.*, 2018). Experiments in mammalian cells suggest that Par3 may help regulate how cells balance apicomedial versus junctional contractility (Zihni *et al.*, 2017). Par3 and ZO-1 are in proximity in mammalian cells (e.g., Van Itallie *et al.*, 2013). How Cno and Pyd act to maintain Baz at AJs remains to be determined: is it via direct interactions or more indirect mechanisms? Together, these data support the idea that loss of cortical Baz in *cno* and *pyd cno* mutants may affect cortical contractility, but the complexity of the context-dependent roles of Baz/Par3 in different contexts leaves questions to be answered in the future. The way in which Cno and Pyd fit into the context-dependent mechanisms that regulate adhesion, polarity, and contractility in different tissues could also be addressed by making clones of cells with reduced Cno and Pyd in other tissues, including the ovarian follicle cells and wing or eye imaginal discs.

Cno and Pyd: cooperative or parallel functions?

Another challenge for future work is defining the mechanisms by which Pyd/ZO-1 and Cno/Afadin act together and/or in parallel. Current data remain somewhat paradoxical. *Drosophila* and mammalian family members can directly bind one another. In mammals, ZO-1 is

Fly stocks	Source
UAS.cnoRNAiV22 (stock #38194)	Bloomington *Drosophila* Stock Center (Bloomington, IL)
UAS.cnoRNAiV20 (stock #33367)	Bloomington *Drosophila* Stock Center (Bloomington, IL)
pyd^{B12}/pyd^{B12} ($pyd^{M/Z}$)	Peifer lab; Choi *et al.* (2011)
cno^{R2}	Peifer lab; Sawyer *et al.* (2009)
EcadGFP (stock #60584)	Bloomington *Drosophila* Stock Center (Bloomington, IL)
ZipGFP (stock #51564)	Bloomington *Drosophila* Stock Center (Bloomington, IL)
Nos-Gal4 (stock #32563)	Bloomington *Drosophila* Stock Center (Bloomington, IL)
MTD-Gal4 (*nos-Gal4;nos-VP16-Gal4;otu-Gal4*) (stock #31777)	Bloomington *Drosophila* Stock Center (Bloomington, IL)
Mat-tub-Gal4;Mat-tub-Gal4 (stock #80361)	Bloomington *Drosophila* Stock Center (Bloomington, IL)
Mat-tub-Gal4 (stock #7062)	Bloomington *Drosophila* Stock Center (Bloomington, IL)

TABLE 2: Fly stocks.

best known for its roles in tight junctions, while Afadin is an AJ protein, suggesting spatial separation—however, experiments using biotin–ligase proximity assessment in MDCK cells suggest that at least some fraction of each protein is in close proximity to the other (Van Itallie *et al.*, 2013). In flies, Cno and Pyd colocalize to AJs. Previous genetic assessments revealed genetic interactions, but these involved either partially functional alleles or knockdown (Yamamoto *et al.*, 1997; Takahashi *et al.*, 1998; Choi *et al.*, 2016)—this made difficult assessment of whether an interaction involves two proteins acting in the same pathway or two proteins operating in separate but parallel pathways. Our current work uses embryos maternally and zygotically null for Pyd, avoiding this ambiguity.

The strong genetic enhancement of *pyd* null embryos by Cno knockdown suggests that the two proteins act, at least in part, in parallel. Another data set supporting the idea that Cno and Pyd act in part in parallel rather than together comes from their respective localizations during germband extension—Pyd is planar polarized along with AJ proteins and Baz on DV boundaries (Supplemental Figure 5, A and B), while Cno is enriched on AP boundaries with actin and myosin (Sawyer *et al.*, 2011). Each could thus reinforce junctions at their respective locations, with combined loss further destabilizing adhesion. Alternately, they could have quite distinct functions: our work in MDCK cells suggests that ZO-1 family proteins can negatively regulate actomyosin assembly and contractility at AJs, by negatively regulating the Rok activator Shroom, while Afadin strengthens junction–cytoskeletal connections under tension (Choi *et al.*, 2016). Intriguingly, Shroom plays a role in the reciprocal planar polarization of myosin and Baz, with its activity elevated at the borders where myosin is elevated and Baz and Pyd are reduced (Simoes Sde *et al.*, 2014). Thus down-regulation of Shroom and thus myosin contractility by Pyd is a possibility in *Drosophila*, though the relatively mild *pyd* and *shroom* single mutant phenotypes (Choi *et al.*, 2011; Simoes Sde *et al.*, 2014) suggest that in flies other proteins play overlapping and partially redundant roles. A different speculative possibility is that Afadin and ZO-1 proteins form part of a single large and multivalent protein complex, but recruit into this complex different, nonredundant partners, making loss of both more deleterious than loss of either one alone. Future work, including superresolution imaging of Pyd and Cno, and identification and functional analysis of different binding partners may help resolve these mechanistic questions, and also help define what other proteins act in parallel or together with them—one intriguing candidate is the mechanosensitive junctional protein Jub/Ajuba (Razzell *et al.*, 2018; Rauskolb *et al.*, 2019). Defining interacting partners and parallel mechanisms for maintaining epithelial integrity is an important future direction.

MATERIALS AND METHODS

Fly stocks

Fly stocks are listed in Table 2. Wild type was *yellow white*, *Histone-GFP*, or *Histone-RFP*. Most experiments were performed at 25°C; we also carried out *cnoS-RNAi* at 27° to potentially increase the severity of knockdown. Mutations are described at Flybase, https://flybase.org/. *shRNA* knockdown of *cno* was carried out by crossing double-copy *mat-tub-GAL4,* single-copy *mat-tub-Gal4*, *nos-Gal4*, or *MTD-Gal4* females to males carrying UAS.*cnoValium20*shRNAi (control experiments for the *pyd* cno double mutants) or UAS*cnoValium22shRNA* constructs. The pyd^{B12} *UAScnoValium20shRNA* (pyd^{B12} *cnoRNAiV20*) chromosome (used to generate *pyd cno* double mutants) was generated through homologous recombination on chromosome 3 using the pyd^{B12} deficiency allele (Choi *et al.*, 2011) and the *UAScno Valium20* allele. pyd^{B12} *cnoRNAiV20* females were then crossed to male single-copy *mat-tub-Gal4;* pyd^{B12}*/TM3* males.

Cuticle preparation

Cuticle preparation was performed according to Wieschaus and Nüsslein-Volhard (1986) with the following modifications. Embryos were collected and allowed to develop for 48 h at 25°C. Unhatched embryos were washed in 0.1% Triton X-100 and dechorionated in 50% bleach for 5 min in a glass depression slide. After being washed once in 0.1% Triton X-100, embryos were mounted in 1:1 diluted Hoyer's medium:lactic acid and incubated at 60°C overnight.

Immunofluorescence

Antibodies and dilutions used are listed in Table 3. All embryos were dechorionated in 50% bleach for 5 min on nutator. Most antibody staining was done on "heat fixed" embryos, which were fixed in boiling Triton salt solution (0.03% Triton X-100, 68 mM NaCl, 8 mM EGTA) for 10 s, followed by fast cooling on ice, and devitellinized by vigorous shaking in 1:1 heptane:methanol. Embryos were stored in 95% methanol/5% 0.5 M EGTA for at least 48 h at –20°C before staining. Embryos were washed three times in blocking solution (0.01% Triton X-100 in PBS; PBS-T) with 1% normal goat serum (NGS), followed by blocking during nutation for 1 h. In select experiments, embryos were formaldehyde fixed in 1:1 4% formaldehyde in phosphate-buffered saline (PBS):heptane for 20 min or 1:1 8% formaldehyde in PBS:heptane for 30 min, while being rocked. Embryos were devitellinized by vigorous shaking in 1:1 heptane:methanol, except when F-actin was visualized using phalloidin, when they were devitellinized using 1:1 heptane:95% ethanol or by manual removal of the vitelline membrane with a scalpel. Primary and secondary antibody staining were each carried out at

Antibodies	Dilution	Source
Immunofluorescence		
Primary antibodies		
Anti-Canoe (rabbit)	1:2000	J. Sawyer and N. Harris (University of North Carolina, Chapel Hill, NC)
Anti-DE-cadherin (rat)	1:50	Developmental Studies Hybridoma Bank (DSHB), (University of Iowa, Iowa City, IA)
Anti-Armadillo (mouse)	1:100	DSHB
Anti-Neurotactin (mouse)	1:100	DSHB
Anti-Enabled (mouse)	1:500	DSHB
Anti-Polychaetoid (mouse)	1:250	Peifer lab; Choi *et al*. (2011)
Anti-Bazooka (rabbit)	1:2000	Peifer lab; Choi *et al*. (2013)
Anti-Nonmuscle myosin II heavy chain (rabbit)	1:500	Jeffrey Thomas (Texas Tech University); Chougule *et al*. (2016)
Secondary antibodies		
AlexaFluor 405,488,568, and 647	1:500	Life Technologies
Phalloidin TRITC and FITC	1:500	Thermo Fisher Scientific
Immunoblotting		
Primary antibodies		
Anti-Armadillo (mouse)	1:500	DSHB
Anti-Canoe (rabbit)	1:1000	J. Sawyer and N. Harris (University of North Carolina, Chapel Hill, NC)
Anti-Polychaetoid (mouse)	1:1000	Peifer lab; Choi *et al*. (2011)
Anti-αTubulin (mouse)	1:5000	Sigma Life Science, T6199
Secondary antibodies		
IRDye 680RD (anti-rabbit)	1:10,000	LI-COR Biosciences
IRDye 800CW (anti-mouse)	1:10,000	LI-COR Biosciences

TABLE 3: Antibodies.

4°C overnight with nutation in 1% NGS in PBS-T. After primary and secondary antibody staining, the embryos were washed three times for 5 min with 0.01% Triton X-100 in PBS (PBS-T).

Image acquisition and manipulation

Fixed embryos were mounted in Aqua-Poly/Mount (Polysciences) and imaged on a confocal laser-scanning microscope (LSM 710 or LSM880, 40 ×/NA 1.3 Plan-Apochromat oil objective, Carl Zeiss). ZEN 2009 software (Carl Zeiss) was used to process images and render *z*-stacks in 3D. Superresolution embryos were imaged on Nikon N-SIM, using SR APO TIRF 100 ×/1.49 NA oil objective. NIS-Elements AR Version 4.51 software 2016 (Nikon) was used to process SIM images and render *z*-stacks in 3D. Photoshop CS6 (Adobe) was used to adjust input levels so that the signal spanned the entire output grayscale and to adjust brightness and contrast. Image processing for SIM imaging is described in Supplemental Figure 2.

Quantification of Ena Puncta area and length

Stacks from mid-stage-13 embryos were acquired with LSM 710, 40 ×/NA 1.3 Plan-Apochromat oil objective, Carl Zeiss. To ensure that the entire leading edge was measured, stacks of 10 planes 0.3 µm apart were used to created maximum intensity projections using ZEN 2009 Lite Edition (Carl Zeiss). The resulting projected image was binarized in ImageJ (Schindelin *et al.*, 2012; Rueden *et al.*, 2017) using the Bernsen Auto Local Threshold feature at radius 75 (Bernsen, 1986; Sezgin and Sankur, 2004) to improve the visibility of the puncta. Area of individual puncta was measured using a wand tool. Length of individual puncta was measured using a line tool (linewidth 3). Measured area and lengths were from three or more experiments.

Quantification of planar polarity

Stacks from stage 7 to early stage 8 embryos were acquired with LSM 710 or LSM880, 40 ×/NA 1.3 Plan-Apochromat oil objective, Carl Zeiss. Mean fluorescence intensities of all borders were measured with ImageJ's line tool (linewidth 3) at 300% zoom. To ensure that the entire apical border was measured, stacks of five planes 0.3 µm apart were used. The ImageJ Stacks>Z project function was used to construct a *Z*-axis sum intensity projection. Background mean intensity was subtracted to obtain the final value for each cell. Borders were sorted by angles (relative to embryo DV axis). AP borders, 0°–29°; DV borders, 60°–90°. Ratios from three or more experiments were averaged.

Immunoblotting

Antibodies and dilutions used are listed in Table 3. Expression levels of Arm protein and knockdown efficiency of Cno and Pyd were measured by immunoblotting embryos 1–4 and 12–15 h old. Embryo lysates were performed according to Bonello *et al.* (2018) with the following modification. The lysis buffer was 1% NP-40, 0.5% Na deoxycholate, 0.1% SDS, 50 mM Tris pH 8.0, 300 mM NaCl, 1.0 mM DTT, Halt protease, phosphatase inhibitor cocktail, and 1 mM EDTA. Lysates were resolved using 7 or 8% SDS–PAGE and transferred to a nitrocellulose membrane. The membranes were incubated with the primary antibody for 2 h at room temperature or overnight at 4°C (see Table 3 for antibody concentrations). The membranes were incubated with secondary antibody for 45 min at room temperature (see Table 3 for antibody concentrations). The signal levels were detected using an Odyssey CLx infrared system (LI-COR Biosciences). Band densitometry was calculated using LI-COR Image Studio.

ACKNOWLEDGMENTS

We are grateful to Zachary Blom and Wangsun Choi for initiating the project, to Teresa Bonello for carrying out myosin staining, to Melissa Greene, Clara Williams, and Halle Ronk for technical assistance, to Ulrich Tepass, Sergio Simoes, Paul Maddox, Teresa Bonello, Amy Gladfelter, Kevin Slep, and Kathryn Reissner for helpful discussions, to the Bloomington Drosophila Stock Center, to Tony Perdue for advice on SIM and confocal imaging, to Daniel Cortes for advice on image quantification, to Jeffrey Thomas at Texas Tech University Health Sciences Center for myosin II heavy chain primary antibody, to Michelle Itano of the Neuroscience Center Microscopy Core and Pablo Ariel of the Microscopy Services Laboratory for advice on 3D imaging, and to Teresa Bonello and members of the Peifer lab for helpful discussions and reading the manuscript. The work was supported by National Institutes of Health (NIH) R35 GM118096 to M.P. L.A.M. was supported by NIH K12 GM000678, K.Z.P.-V. by NIH R25 GM055336 and T32 GM007092, and M.T.S. by a diversity supplement on NIH R35 GM118096. M.T.S. was a participant in the UNC PREP Program, which is funded by NIH R25 GM089569.

REFERENCES

Bernsen J (1986). Dynamic thresholding of grey-level images. Proc 8th Int Conf Pattern Recognition.

Bertet C, Sulak L, Lecuit T (2004). Myosin-dependent junction remodelling controls planar cell intercalation and axis elongation. Nature 429, 667–671.

Blankenship JT, Backovic ST, Sanny JS, Weitz O, Zallen JA (2006). Multicellular rosette formation links planar cell polarity to tissue morphogenesis. Dev Cell 11, 459–470.

Boettner B, Harjes P, Ishimaru S, Heke M, Fan HQ, Qin Y, Van Aelst L, Gaul U (2003). The AF-6 homolog Canoe acts as a Rap1 effector during dorsal closure of the *Drosophila* embryo. Genetics 165, 159–169.

Bonello TT, Perez-Vale KZ, Sumigray KD, Peifer M (2018). Rap1 acts via multiple mechanisms to position Canoe and adherens junctions and mediate apical–basal polarity establishment. Development 145, dev157941.

Brand AH, Perrimon N (1993). Targeted gene expression as a means of altering cell fates and generating dominant phenotypes. Development 118, 401–415.

Cheeks RJ, Canman JC, Gabriel WN, Meyer N, Strome S, Goldstein B (2004). *C. elegans* PAR proteins function by mobilizing and stabilizing asymmetrically localized protein complexes. Curr Biol 14, 851–862.

Choi W, Acharya BR, Peyret G, Fardin MA, Mege RM, Ladoux B, Yap AS, Fanning AS, Peifer M (2016). Remodeling the zonula adherens in response to tension and the role of Afadin in this response. J Cell Biol 213, 243–260.

Choi W, Jung KC, Nelson KS, Bhat MA, Beitel GJ, Peifer M, Fanning AS (2011). The single *Drosophila* ZO-1 protein Polychaetoid regulates embryonic morphogenesis in coordination with Canoe/Afadin and Enabled. Mol Biol Cell 22, 2010–2030.

Choi W, Harris NJ, Sumigray KD, Peifer M (2013). Rap1 and Canoe/afadin are essential for establishment of apical-basal polarity in the *Drosophila* embryo. Mol Biol Cell 24, 945–963.

Chougule AB, Hastert MC, Thomas JH (2016). Drak is required for actomyosin organization during drosophila cellularization. G3 (Bethesda) 6, 819–828.

Cox RT, Kirkpatrick C, Peifer M (1996). Armadillo is required for adherens junction assembly, cell polarity, and morphogenesis during *Drosophila* embryogenesis. J Cell Biol 134, 133–148.

David DJ, Tishkina A, Harris TJ (2010). The PAR complex regulates pulsed actomyosin contractions during amnioserosa apical constriction in Drosophila. Development 137, 1645–1655.

Dickinson DJ, Schwager F, Pintard L, Gotta M, Goldstein B (2017). A single-cell biochemistry approach reveals PAR complex dynamics during cell polarization. Dev Cell 42, 416–434 e411.

Djiane A, Shimizu H, Wilkin M, Mazleyrat S, Jennings MD, Avis J, Bray S, Baron M (2011). Su(dx) E3-Ubiquitin ligase dependent and independent functions of Polychaetoid, the *Drosophila* ZO-1 homologue. J Cell Biol 192, 189–200.

Ducuing A, Vincent S (2016). The actin cable is dispensable in directing dorsal closure dynamics but neutralizes mechanical stress to prevent scarring in the *Drosophila* embryo. Nat Cell Biol 18, 1149–1160.

Duffy JB (2002). GAL4 system in *Drosophila*: a fly geneticist's Swiss army knife. Genesis 34, 1–15.

Durney CH, Harris TJC, Feng JJ (2018). Dynamics of PAR proteins explain the oscillation and ratcheting mechanisms in dorsal closure. Biophys J 115, 2230–2241.

Edwards M, Zwolak A, Schafer DA, Sept D, Dominguez R, Cooper JA (2014). Capping protein regulators fine-tune actin assembly dynamics. Nat Rev Mol Cell Biol 15, 677–689.

Fanning AS, Anderson JM (2009). Zonula occludens-1 and -2 are cytosolic scaffolds that regulate the assembly of cellular junctions. Ann NY Acad Sci 1165, 113–120.

Fanning AS, Van Itallie CM, Anderson JM (2012). Zonula occludens-1 and -2 regulate apical cell structure and the zonula adherens cytoskeleton in polarized epithelia. Mol Biol Cell 23, 577–590.

Fernandez-Gonzalez R, Simoes Sde M, Roper JC, Eaton S, Zallen JA (2009). Myosin II dynamics are regulated by tension in intercalating cells. Dev Cell 17, 736–743.

Fernandez-Gonzalez R, Zallen JA (2009). Cell mechanics and feedback regulation of actomyosin networks. Sci Signal 2, pe78.

Foe VE (1989). Mitotic domains reveal early commitment of cells in *Drosophila* embryos. Development 107, 1–22.

Franke JD, Montague RA, Kiehart DP (2005). Nonmuscle myosin II generates forces that transmit tension and drive contraction in multiple tissues during dorsal closure. Curr Biol 15, 2208–2221.

Gates J, Mahaffey JP, Rogers SL, Emerson M, Rogers EM, Sottile SL, Van Vactor D, Gertler FB, Peifer M (2007). Enabled plays key roles in embryonic epithelial morphogenesis in *Drosophila*. Development 134, 2027–2039.

Harris KP, Tepass U (2008). Cdc42 and Par proteins stabilize dynamic adherens junctions in the *Drosophila* neuroectoderm through regulation of apical endocytosis. J Cell Biol 183, 1129–1143.

Harris TJ, Peifer M (2007). aPKC controls microtubule organization to balance adherens junction symmetry and planar polarity during development. Dev Cell 12, 727–738.

Harris TJC (2018). Sculpting epithelia with planar polarized actomyosin networks: principles from *Drosophila*. Semin Cell Dev Biol 81, 54–61.

Hayes P, Solon J (2017). *Drosophila* dorsal closure: an orchestra of forces to zip shut the embryo. Mech Dev 144, 2–10.

Heer NC, Martin AC (2017). Tension, contraction and tissue morphogenesis. Development 144, 4249–4260.

Hutson MS, Tokutake Y, Chang MS, Bloor JW, Venakides S, Kiehart DP, Edwards GS (2003). Forces for morphogenesis investigated with laser microsurgery and quantitative modeling. Science 300, 145–149.

Ikenouchi J, Umeda K, Tsukita S, Furuse M, Tsukita S (2007). Requirement of ZO-1 for the formation of belt-like adherens junctions during epithelial cell polarization. J Cell Biol 176, 779–786.

Jacinto A, Wood W, Woolner S, Hiley C, Turner L, Wilson C, Martinez-Arias A, Martin P (2002). Dynamic analysis of actin cable function during *Drosophila* dorsal closure. Curr Biol 12, 1245–1250.

Jung AC, Ribeiro C, Michaut L, Certa U, Affolter M (2006). Polychaetoid/ZO-1 is required for cell specification and rearrangement during *Drosophila* tracheal morphogenesis. Curr Biol 16, 1224–1231.

Jürgens G, Wieschaus E, Nüsslein-Volhard C, Kluding H (1984). Mutations affecting the pattern of the larval cuticle in *Drosophila melanogaster*: II. Zygotic loci on the third chromosome. Roux's Arch Dev Biol 193, 283–295.

Kaltschmidt JA, Lawrence N, Morel V, Balayo T, Fernandez BG, Pelissier A, Jacinto A, Martinez Arias A (2002). Planar polarity and actin dynamics in the epidermis of *Drosophila*. Nat Cell Biol 4, 937–944.

Katsuno T, Umeda K, Matsui T, Hata M, Tamura A, Itoh M, Takeuchi K, Fujimori T, Nabeshima Y, Noda T, *et al*. (2008). Deficiency of zonula occludens-1 causes embryonic lethal phenotype associated with defected yolk sac angiogenesis and apoptosis of embryonic cells. Mol Biol Cell 19, 2465–2475.

Kiehart DP, Crawford JM, Aristotelous A, Venakides S, Edwards GS (2017). Cell sheet morphogenesis: dorsal closure in *Drosophila melanogaster* as a model system. Annu Rev Cell Dev Biol 33, 169–202.

Kiehart DP, Galbraith CG, Edwards KA, Rickoll WL, Montague RA (2000). Multiple forces contribute to cell sheet morphogenesis for dorsal closure in *Drosophila*. J Cell Biol 149, 471–490.

Knox AL, Brown NH (2002). Rap1 GTPase regulation of adherens junction positioning and cell adhesion. Science 295, 1285–1288.

Kong D, Wolf F, Grosshans J (2017). Forces directing germ-band extension in *Drosophila* embryos. Mech Dev 144, 11–22.

Levayer R, Pelissier-Monier A, Lecuit T (2011). Spatial regulation of Dia and Myosin-II by RhoGEF2 controls initiation of E-cadherin endocytosis during epithelial morphogenesis. Nat Cell Biol 13, 529–540.

Maitre JL, Heisenberg CP (2011). The role of adhesion energy in controlling cell–cell contacts. Curr Opin Cell Biol 23, 508–514.
Maitre JL, Heisenberg CP (2013). Three functions of cadherins in cell adhesion. Curr Biol 23, R626–633.
Mandai K, Rikitake Y, Shimono Y, Takai Y (2013). Afadin/AF-6 and canoe: roles in cell adhesion and beyond. Prog Mol Biol Transl Sci 116, 433–454.
Mazzalupo S, Cooley L (2006). Illuminating the role of caspases during *Drosophila* oogenesis. Cell Death Differ 13, 1950–1959.
Mege RM, Ishiyama N (2017). Integration of cadherin adhesion and cytoskeleton at adherens junctions. Cold Spring Harb Perspect Biol 9, a028738.
Meng W, Takeichi M (2009). Adherens junction: molecular architecture and regulation. Cold Spring Harb Perspect Biol 1, a002899.
Miyamoto H, Nihonmatsu I, Kondo S, Ueda R, Togashi S, Hirata K, Ikegami Y, Yamamoto D (1995). *canoe* encodes a novel protein containing a GLGF/DHR motif and functions with *Notch* and *scabrous* in common developmental pathways in *Drosophila*. Genes Dev 9, 612–625.
Müller H-AJ, Wieschaus E (1996). *armadillo*, *bazooka*, and *stardust* are critical for formation of the zonula adherens and maintenance of the polarized blastoderm epithelium in *Drosophila*. J Cell Biol 134, 149–165.
Munro E, Nance J, Priess JR (2004). Cortical flows powered by asymmetrical contraction transport PAR proteins to establish and maintain anterior-posterior polarity in the early *C. elegans* embryo. Dev Cell 7, 413–424.
Nowotarski SH, McKeon N, Moser RJ, Peifer M (2014). The actin regulators Enabled and Diaphanous direct distinct protrusive behaviors in different tissues during *Drosophila* development. Mol Biol Cell 25, 3147–3165.
O'Keefe DD, Gonzalez-Nino E, Burnett M, Dylla L, Lambeth SM, Licon E, Amesoli C, Edgar BA, Curtiss J (2009). Rap1 maintains adhesion between cells to affect Egfr signaling and planar cell polarity in *Drosophila*. Dev Biol 333, 143–160.
O'Keefe DD, Gonzalez-Nino E, Edgar BA, Curtiss J (2012). Discontinuities in Rap1 activity determine epithelial cell morphology within the developing wing of *Drosophila*. Dev Biol 369, 223–234.
Ozawa M (1998). Identification of the region of alpha-catenin that plays an essential role in cadherin-mediated cell adhesion. J Biol Chem 273, 29524–29529.
Pasakarnis L, Frei E, Caussinus E, Affolter M, Brunner D (2016). Amnioserosa cell constriction but not epidermal actin cable tension autonomously drives dorsal closure. Nat Cell Biol 18, 1161–1172.
Perkins LA, Holderbaum L, Tao R, Hu Y, Sopko R, McCall K, Yang-Zhou D, Flockhart I, Binari R, Shim HS, *et al*. (2015). The Transgenic RNAi Project at Harvard Medical School: resources and validation. Genetics 201, 843–852.
Pinheiro D, Hannezo E, Herszterg S, Bosveld F, Gaugue I, Balakireva M, Wang Z, Cristo I, Rigaud SU, Markova O, Bellaiche Y (2017). Transmission of cytokinesis forces via E-cadherin dilution and actomyosin flows. Nature 545, 103–107.
Rauskolb C, Cervantes E, Madere F, Irvine KD (2019). Organization and function of tension-dependent complexes at adherens junctions. J Cell Sci 132, jcs224063.
Razzell W, Bustillo ME, Zallen JA (2018). The force-sensitive protein Ajuba regulates cell adhesion during epithelial morphogenesis. J Cell Biol 217, 3715–3730.
Rimm DL, Koslov ER, Kebriaei P, Cianci CD, Morrow JS (1995). Alpha 1(E)-catenin is an actin-binding and -bundling protein mediating the attachment of F-actin to the membrane adhesion complex. Proc Natl Acad Sci USA 92, 8813–8817.
Rodriguez J, Peglion F, Martin J, Hubatsch L, Reich J, Hirani N, Gubieda AG, Roffey J, Fernandes AR, St Johnston D, *et al*. (2017). aPKC cycles between functionally distinct PAR protein assemblies to drive cell polarity. Dev Cell 42, 400–415.e409.
Rueden CT, Schindelin J, Hiner M (2017). ImageJ2: ImageJ for the next generation of scientific image data. BMC Bioinformatics 18, 529.
Sarpal R, Pellikka M, Patel RR, Hui FY, Godt D, Tepass U (2012). Mutational analysis supports a core role for *Drosophila* alpha-catenin in adherens junction function. J Cell Sci 125, 233–245.
Sawyer JK, Choi W, Jung KC, He L, Harris NJ, Peifer M (2011). A contractile actomyosin network linked to adherens junctions by Canoe/afadin helps drive convergent extension. Mol Biol Cell 22, 2491–2508.
Sawyer JK, Harris NJ, Slep KC, Gaul U, Peifer M (2009). The *Drosophila* Afadin homologue Canoe regulates linkage of the actin cytoskeleton to adherens junctions during apical constriction. J Cell Biol 186, 57–73.
Schindelin J, Arganda-Carrera I, Frise E, Kaynig V, Longair M, Pietzsch T, Preibisch S, Rueden C, Saalfeld S, Schmid B, *et al*. (2012). Fiji: an open-source platform for biological-image analysis. Nat Methods 9, 676–682.
Seppa MJ, Johnson RI, Bao S, Cagan RL (2008). Polychaetoid controls patterning by modulating adhesion in the *Drosophila* pupal retina. Dev Biol 318, 1–16.
Sezgin M, Sankur B (2004). Survey over image thresholding techniques and quantitative performance evaluation. J Electronic Imaging 13, 146–165.
Simoes Sde M, Blankenship JT, Weitz O, Farrell DL, Tamada M, Fernandez-Gonzalez R, Zallen JA (2010). Rho-kinase directs Bazooka/Par-3 planar polarity during *Drosophila* axis elongation. Dev Cell 19, 377–388.
Simoes Sde M, Mainieri A, Zallen JA (2014). Rho GTPase and Shroom direct planar polarized actomyosin contractility during convergent extension. J Cell Biol 204, 575–589.
Staller MV, Yan D, Randklev S, Bragdon MD, Wunderlich ZB, Tao R, Perkins LA, Depace AH, Perrimon N (2013). Depleting gene activities in early *Drosophila* embryos with the "maternal-Gal4-shRNA" system. Genetics 193, 51–61.
Takahashi K, Matsuo T, Katsube T, Ueda R, Yamamoto D (1998). Direct binding between two PDZ domain proteins Canoe and ZO-1 and their roles in regulation of the jun N-terminal kinase pathway in *Drosophila* morphogenesis. Mech Dev 78, 97–111.
Takahisa M, Togashi S, Suzuki T, Kobayashi M, Murayama A, Kondo K, Miyake T, Ueda R (1996). The *Drosophila* tamou gene, a component of the activating pathway of extramacrochaetae expression, encodes a protein homologous to mammalian cell-cell junction-associated protein ZO-1. Genes Dev 10, 1783–1795.
Tamada M, Farrell DL, Zallen JA (2012). Abl regulates planar polarized junctional dynamics through beta-catenin tyrosine phosphorylation. Dev Cell 22, 309–319.
Tepass U, Gruszynski-DeFeo E, Haag TA, Omatyar L, Török T, Hartenstein V (1996). *shotgun* encodes *Drosophila* E-cadherin and is preferentially required during cell rearrangement in the neuroectoderm and other morphogenetically active epithelia. Genes Dev 10, 672–685.
Tetley RJ, Mao YL (2018). The same but different: cell intercalation as a driver of tissue deformation and fluidity. Philos T R Soc B 373, 20170328.
Toyama Y, Peralta XG, Wells AR, Kiehart DP, Edwards GS (2008). Apoptotic force and tissue dynamics during *Drosophila* embryogenesis. Science 321, 1683–1686.
Umeda K, Ikenouchi J, Katahira-Tayama S, Furuse K, Sasaki H, Nakayama M, Matsui T, Tsukita S, Furuse M, Tsukita S (2006). ZO-1 and ZO-2 independently determine where claudins are polymerized in tight-junction strand formation. Cell 126, 741–754.
Van Itallie CM, Anderson JM (2014). Architecture of tight junctions and principles of molecular composition. Semin Cell Dev Biol 36, 157–165.
Van Itallie CM, Aponte A, Tietgens AJ, Gucek M, Fredriksson K, Anderson JM (2013). The N and C termini of ZO-1 are surrounded by distinct proteins and functional protein networks. J Biol Chem 288, 13775–13788.
Vichas A, Zallen JA (2011). Translating cell polarity into tissue elongation. Semin Cell Dev Biol 22, 858–864.
Wang SC, Low TYF, Nishimura Y, Gole L, Yu W, Motegi F (2017). Cortical forces and CDC-42 control clustering of PAR proteins for *Caenorhabditis elegans* embryonic polarization. Nat Cell Biol 19, 988–995.
Wei X, Ellis HM (2001). Localization of the *Drosophila* MAGUK protein Polychaetoid is controlled by alternative splicing. Mech Dev 100, 217–231.
Weng M, Wieschaus E (2016). Myosin-dependent remodeling of adherens junctions protects junctions from Snail-dependent disassembly. J Cell Biol 212, 219–229.
Weng M, Wieschaus E (2017). Polarity protein Par3/Bazooka follows myosin-dependent junction repositioning. Dev Biol 422, 125–134.
Wieschaus E, Nüsslein-Volhard C (1986). Looking at embryos. In: Drosophila, A Practical Approach, ed. D.B. Roberts, Oxford, UK: IRL Press, 199–228.
Winklbauer R (2015). Cell adhesion strength from cortical tension—an integration of concepts. J Cell Sci 128, 3687–3693.
Xu J, Kausalya PJ, Phua DC, Ali SM, Hossain Z, Hunziker W (2008). Early embryonic lethality of mice lacking ZO-2, but not ZO-3, reveals critical and nonredundant roles for individual zonula occludens proteins in mammalian development. Mol Cell Biol 28, 1669–1678.
Yamamoto T, Harada N, Kano K, Taya S, Canaani E, Matsuura Y, Mizoguchi A, Ide C, Kaibuchi K (1997). The Ras target AF-6 interacts with ZO-1 and serves as a peripheral component of tight junctions in epithelial cells. J Cell Biol 139, 785–795.
Yamazaki Y, Umeda K, Wada M, Nada S, Okada M, Tsukita S, Tsukita S (2008). ZO-1- and ZO-2-dependent integration of myosin-2 to epithelial zonula adherens. Mol Biol Cell 19, 3801–3811.
Yan L, Bi DP (2019). Multicellular rosettes drive fluid–solid transition in epithelial tissues. Phys Rev X 9, 011029.
Zallen JA, Wieschaus E (2004). Patterned gene expression directs bipolar planar polarity in *Drosophila*. Dev Cell 6, 343–355.
Zihni C, Vlassaks E, Terry S, Carlton J, Leung TKC, Olson M, Pichaud F, Balda MS, Matter K (2017). An apical MRCK-driven morphogenetic pathway controls epithelial polarity. Nat Cell Biol 19, 1049–1060.